TGF-β blockade drives a transitional effector phenotype in T cells reversing SIV latency and decreasing SIV reservoirs in vivo

Jinhee Kim[1], Deepanwita Bose[2]†, Mariluz Araínga[2]†, Muhammad R. Haque[3], Christine M Fennessey[4], Rachel A Caddell[5], Yanique Thomas[3], Douglas E Ferrell[2], Syed Ali[2], Emanuelle Grody[3,9], Yogesh Goyal[3,9,10], Claudia Cicala[6], James Arthos[6], Brandon F Keele[4], Monica Vaccari[5,7], Ramon Lorenzo-Redondo[1,8], Thomas J Hope[3], Francois Villinger[2] and Elena Martinelli[1]

[1]Department of Medicine, Division of Infectious Diseases, Feinberg School of Medicine, Northwestern University, Chicago, IL, USA
[2]New Iberia Research Center, University of Louisiana at Lafayette, New Iberia, LA, USA
[3]Cell and Developmental Biology, Feinberg School of Medicine, Northwestern University, Chicago, IL, USA
[4]AIDS and Cancer Virus Program, Frederick National Laboratory for Cancer Research, Frederick MD
[5]Division of Immunology, Tulane National Primate Research Center, Covington LA, USA
[6]Laboratory of Immunoregulation, National Institute of Allergy and Infectious Diseases, National Institutes of Health, Bethesda, MD, USA
[7]Department of Microbiology and Immunology, Tulane University School of Medicine, New Orleans, LA, USA
[8]Center for Pathogen Genomics and Microbial Evolution, Northwestern University Havey Institute for Global Health, Chicago, IL, USA.
[9]Center for Synthetic Biology, Northwestern University, Chicago, IL, USA
[10]Robert H. Lurie Comprehensive Cancer Center, Feinberg School of Medicine, Northwestern University, Chicago, IL, USA

*Corresponding author:

Elena Martinelli

elena.martinelli@northwestern.edu

One-sentence summary:

TGF-β blockade drives an effector phenotype in immune cells leading to SIV latency reversal and enhanced immune responses in vivo.

36

Abstract

HIV-1 persistence during ART is due to the establishment of long-lived viral reservoirs in resting immune cells. Using an NHP model of barcoded SIVmac239 intravenous infection and therapeutic dosing of the anti-TGFBR1 inhibitor galunisertib (LY2157299), we confirmed the latency reversal properties of *in vivo* TGF-β blockade, decreased viral reservoirs and stimulated immune responses. Eight SIV-infected macaques on suppressive ART were treated with 4 2-week cycles of galunisertib. ART was discontinued 3 weeks after the last dose, and macaques euthanized 6 weeks after ART-interruption(ATI). One macaque did not rebound, while the remaining rebounded between week 2 and 6 post-ATI. Galunisertib led to viral reactivation as indicated by plasma viral load and immunoPET/CT with the ^{64}Cu-DOTA-F(ab')$_2$-p7D3-probe. Half to 1 Log decrease in cell-associated (CA-)SIV DNA was detected in lymph nodes, gut and PBMC, while intact pro-virus in PBMC decreased by 3-fold. No systemic increase in inflammatory cytokines was observed. High-dimensions cytometry, bulk and single-cell RNAseq revealed a shift toward an effector phenotype in T and NK cells.

In summary, we demonstrated that galunisertib, a clinical stage TGF-β inhibitor, reverses SIV latency and decreases SIV reservoirs by driving T cells toward an effector phenotype, enhancing immune responses *in vivo* in absence of toxicity.

Introduction

Interruption of antiretroviral therapy (ART) leads to rapid rebound of viremia in the vast majority of people living with HIV-1 (PLWH) due to the establishment of a persistent HIV-1 reservoir early after infection(*1, 2*). A key mechanism of this persistence is the ability of HIV-1 to enter a state of virological latency characterized by the silencing of viral gene expression and/or lack of viral proteins translation(*3, 4*). This allows the virus to remain invisible to the immune system and latently infected cells to survive and proliferate by homeostatic or antigen-driven proliferation(*5, 6*). Of note, the viral reservoir was initially thought to be stable. However, recent evidence suggests that stochastic HIV reactivation under ART occurs, and selective killing is favored in cells bearing replication competent virus integrated in transcriptionally active sites within the genome(*7-9*). Hence, integration site, but especially the activation status of the infected cells profoundly influences HIV-1 persistence.

Ongoing efforts to achieve a functional cure for HIV-1 are directed towards supplementing ART with immunotherapies targeting the viral reservoir. Such strategies, under the umbrella of “shock and kill”, aim to reactivate the replication competent reservoir and eliminate latently infected cells by viral cytopathic effects or immune-mediated killing (*10, 11*). However, these strategies have thus far failed to achieve a reduction of the viral reservoir or post-ART virologic control in either the clinic or preclinical models. This is mainly due to the low inducibility of latent proviruses and the heterogeneity of the mechanisms of persistence(*12, 13*) (*14, 15*). In contrast, therapeutic vaccination strategies focused on enhancing HIV/SIV-specific responses have had some discreet measure of success(*16*). However, currently, no single strategy leads simultaneously to latency reversal and stimulation of effective immune responses.

The HIV life cycle and HIV’s ability to replicate efficiently are especially dependent on the activation status of the infected cells. In this context, significant advances have been made to directly activate immune cells through non-canonical pathways in order to promote HIV latency reversal(*17*). However, the activation and differentiation of immune cells is intrinsically linked to

cellular metabolism(*18*). Indeed, signaling pathways that govern immune cell differentiation and activation such as mTOR and Wnt/β-catenin, not only have been implicated in regulating HIV latency(*19-21*), but are also critical regulators of cell metabolism(*22*). The metabolic status of an infected cell, in turn, plays a critical role in its ability to support latency reactivation and viral production(*19, 23*).

In this context, recent evidence suggests that TGF-β plays a critical role in the regulation of immune cell activation and metabolic reprogramming(*24-26*). Specifically, in the context of $CD8^+$ T cells, TGF-β has been shown to suppress mTOR signaling preserving the metabolic fitness of memory $CD8^+$ T cells(*25*) and stem-like antigen specific $CD8^+$ T cells through its modulation of Wnt/β-catenin factor TCF1(*26, 27*). TCF1 and the mTOR pathway are also critical to T cell differentiation and responsible for the transition from activated effector cells to resting memory cells during LCMV infection(*22, 26*). The regulation of quiescence in $CD8^+$ T cells that follows continuous TGF-β stimulation is critical to the transition to a memory phenotype and it is driven by specific metabolic changes that are linked to decreased glycolytic activity, more efficient mitochondrial respiration, and long-term survival(*25, 26*).

Similarly, in the context of NK cells, TGF-β has been implicated in decreasing their baseline metabolism driving lower expression of markers of NK cytotoxic activity(*28*).

While TGF-β-mediated suppression of TCR and IL-2 signaling were shown to lead to lower $CD4^+$ T cell activation following cognate antigen recognition in older studies(*24, 29*), more recent work using $CD4^+$ T cell-specific deletion of the TGF-β receptor demonstrated an even more profound effect of TGF-β on all stages of $CD4^+$ T cell activation, proliferation and cytotoxic response to LCMV than in $CD8^+$ T cells(*30*). However, little is known on the specific role of TGF-β in regulating the transition to and from memory and effector phenotypes in $CD4^+$ T cells and how this may be associated with TGF-β-driven changes in $CD4^+$ T cells metabolism. Moreover, TGF-β regulates the expression of CD103 and other surface and intracellular factors

essential of T cell residency in mucosal tissues(*31-33*). Hence, TGF-β is considered the master regulator of mucosal immunity(*34*).

We and others have recently demonstrated that TGF-β regulates HIV-1 latency in primary $CD4^+$ T cells ex vivo and in vivo(*35-37*). Latency reversal was detected in a non-human primate (NHP) model of HIV infection following a short treatment with a clinical stage TGF-β inhibitor, galunisertib (LY2157299)(*38*). In that previous study, we documented latency reversal particularly at the level of the gut mucosal tissue using the ^{64}Cu-anti-gp120 Fab_2(7D3) probe and immuno-PET/CT(*35*). In that study, we further validated the ability of immune-PET/CT to identify sites of viral reactivation and replication in the gut by performing tissue resection in hot areas of the gut identified by PET followed by confirmatory PCR for vDNA/RNA and vRNAscope(*35*).

Herein, we demonstrate how treatment with galunisertib with a 2-week on, 2-week off regiment that mimics the therapeutic regimen employed in the clinic in phase 1 and 2 trials of solid tumors(*39, 40*), leads to profound transcriptional and functional changes in immune cells in the absence of overt toxicity or increased systemic inflammation. Importantly, we observed a shift toward a transitional effector phenotype in $CD4^+$ T cells and other immune cells both systemically and in the lymph nodes. This shift was accompanied by, and likely responsible for, increased viral reactivation in SIV-infected, ART treated macaques documented by molecular techniques and PET/CT images. At the end of the treatment with galunisertib, we detected lower viral reservoir levels, including total and intact proviral DNA in both PBMC, gut and lymph nodes and significantly higher immune responses.

RESULTS

2-weeks on-off therapeutic regiment with Galunisertib leads to viral reactivation SIV infected, ART-treated macaques.

To confirm galunisertib-driven HIV/SIV latency reversal and investigate the underlying mechanisms, 8 Indian origin rhesus macaques (*Macaca Mulatta*, Mamu-A01-, -B08, -B17-, all females) were infected intravenously with 300 TCID50 of the barcoded SIVmac239M2. We initiated ART treatment (daily co-formulated Tenofovir [PMPA], Emtricitabine [FTC] and Dolutegravir [DTG]) on week 6 post-infection (pi). A 2-week on, 2-week off therapeutic cycle with galunisertib (20mg/Kg twice/daily orally) started at week ~35pi and continued for a total of 4 cycles (Fig 1A and Table S1). ART was discontinued 3 weeks after the last galunisertib dose, and the macaques were followed for 6 weeks after ART discontinuation. Median peak plasma viral load (pVL) was 10^8 copies/ml at week 2pi. A rhesus anti-PD1 antibody was administered at 5mg/kg before the 3rd and 4th cycle to 2 macaques (08M156 and A6X003). However, no differences were noted for these 2 macaques in any of the parameters we measured, and the data were pooled.

Full suppression to undetectable levels (pVL LOD 15 copies/ml) was achieved in 3 out of the 8 macaques at week 10pi. In the other 5 macaques, pVL fell below 65 copies/ml by week 22pi with a single blip of 400 copies/ml in A8T010 at week 29pi (Fig 1B). Following the start of the galunisertib treatment, pVLs increased in 7 out of 8 macaques from a single peak over undetectable in 08M171 and A8L057 to several peaks and up to 10^3 copies/ml in the other macaques. Of note pVLs in A8T010 and A8R095 was undetectable for over 5 weeks before, respectively, blips of up to 10^2 copies/ml were detected following galunisertib treatment initiation (Fig 1B). More frequent blips were noted during the first 2 cycles with galunisertib compared to cycles 3 and 4 (Fig 1C). However, 08M171 and A8L057 did not experience a pVL increase until the 4th cycle.

Importantly, we documented viral reactivation also using immunoPET/CT. The ^{64}Cu-anti-gp120 Fab_2(7D3) probe was injected 24hrs before and after, respectively, the beginning and the end of the first 3 galunisertib cycles and scans performed before and after the first and the last dose. As shown in Fig 2, Fig S1 and Movies S1-S8, the PET signal visibly increased in different areas

after cycle 2 (in A8R095, 08M156, A8L014 and A8T010) or at the beginning of cycle 3 (in A6X003, 08M134 and A8L057). In 08M171 we observed an increase in the gut area only at the beginning of cycle 2. A corresponding increase in standard uptake values (SUV) was detected in the gastrointestinal area and axillary lymph nodes (Fig 2B) and was significant in cycle 3 compared to before cycle 1 (BC1). In these anatomical areas, SUV increases correspond to increases in viral replication as shown in previous studies(*41, 42*). A PET signal increase was also noted in the area of the vertebral column (spine). Spine SUV already increased significantly with the first cycle (Fig 2B). However, neither cerebrospinal fluid (CSF) nor bone marrow (BM) was collected during the study, and we have no prior validation of the specificity of the signal in the spine. Hence, whether this signal corresponds to increased viral replication and whether this occurs in the vertebral bones or cerebrospinal fluids remains to be determined. No SUV increase was present at the level of the spleen or kidney, where probe accumulation and background signal likely masked any specific signal. However, a significant increase in SUV was detected in the liver (Fig 2B) and whole-body (Fig S2). Of note, the SUV increase in the gut area in most cases followed an increase in cell-associated vRNA detected in colorectal biopsies at the same time points during treatment (Fig S3).

A 4 cycle treatment with galunisertib decreases viral reservoir in absence of systemic inflammation.

To determine the impact of galunsiertib on SIV reservoir, we measured CA-vDNA in PBMC, colorectal biopsies and lymph nodes (LN). A significant decrease in CA-vDNA was detected in all tissues between week 35pi (beginning of cycle 1, BC1) and week 49pi (after/end of cycle 4, AC4) for gut and LN, and between week 35pi (BC1) and end of cycle 3 (AC3) for PBMC (Fig 3A, AC4 not measured for PBMC and Fig S4A). In the gut and LN (right axillary), decreases ranged from a Log to 1/3 of a Log (gut: median 0.77; range:0.33-0.94 folds LN: median: 0.93; range:0.33-0.98 folds decrease). In the PBMC the decrease was slightly less pronounced with a

median half Log decrease (median: 0.58; range 0.28-0.88 folds decrease). However, the comparison for the PBMCs was between week ~35 and week ~45 (end of cycle 3, AC3) instead of the end of all 4 cycles, because a snap frozen pellet was not available at the end of cycle 4 for PBMCs. The SIV reservoir in PBMCs was also monitored by SIV-IPDA comparing before cycle 1 (BC1) to the end of cycle 4 (AC4). Of note, we observed significant decreases of both total and intact provirus by SIV-IPDA. Intact provirus declined similarly to the CA-vDNA with a median of half Log (median: 0.53; range:0-0.71 folds decrease).

In contrast, no decline in CA-vDNA was detected in the PBMCs of a group of 4 macaques infected intravenously with the same stock of SIVmac239M2 for a separate study. These 4 macaques were placed on ART on week 6pi as in our study. However, no decline in CA-vDNA was detected under ART, between weeks 28 and 52pi (untreated group, Fig S4B). Thus, we conclude that the decline in CA-vDNA in PBMC was not due to ART-alone.

Importantly, we found no significant changes in any of the clinical variables (chemistry and hematology, Tables S2 and S3) measured before, during and after the galunisertib therapy. Moreover, we observed no changes in the concentrations of inflammatory chemokines and cytokines measured in plasma before and after the first 2 treatment cycles and at the end of the last cycle (Fig 3C). The only difference in cytokine and chemokine levels after galunisertib treatment was a small increase in IL-10 detected at the end of the last cycle compared to before treatment (Fig S4C).

Galunisertib treatment drives an effector phenotype in T and NK cells.

The phenotype of PBMCs before and after Galunisertib treatment was monitored by high-parameter flow cytometry of T and NK cell subsets and phenotype (Table S4). Classical subsets and single-color analysis of MFI revealed a substantial increase in the expression of CD95 and a profound consistent decrease in TCF1 expression in $CD4^+$ T cells that continued throughout the treatment (Fig 4A). In contrast, a small decrease in CD62L after the first cycle, reverted to

baseline during the following cycles. The frequency of naïve cells, defined as $CD95^-$ within $CD4^+$ T cells, decreased in parallel with the increase in CD95 (gating strategy in Fig S5). Interestingly, there was no change in the expression of CCR7 or CD28 within $CD95^+$ $CD4^+$ T cells (Fig 4B). Hence, the frequency of central memory and effector memory as defined by CD95 and CD28 or CCR7 did not change (Table S5). The levels of T-bet did not change significantly (Fig S6A). However, we detected a downregulation of the gut homing receptor integrin $\alpha4\beta7$ and a decrease in the levels of granzyme B (GRZB, Fig S6A). Of note, the expression of activation markers CD69, HLA-DR and Ki67 remained mostly unchanged, with the exception of an increase in HLA-DR at the beginning of cycle 2 compared to before galunisertib (Fig 4C). Interestingly, the effect of Galunisertib on $CD8^+$ T cells was not as pronounced as it was on $CD4^+$ T cells. No significant increase was detected in CD95 expression and TCF1 downregulation reached significance only at the end of the treatment (Fig 4D). Markers of cell activation like HLA-DR, Ki67 and CD69 did not change (Fig 4D and Fig S6B). However, we detected a significant decrease in T-Bet at the beginning of cycle 2 (BC2) compared to before treatment (BC1). Finally, in contrast to $CD4^+$ T cells, the decrease in GRZB was more pronounced at several time points during treatment and there was a sustained significant increase in CCR7 expression in memory $CD8^+$ T cells (Fig 4E). Interestingly, the expression of PD1 on both $CD4^+$ T cells and $CD8^+$ T cells either did not change or was slightly downregulated. Importantly, the frequency of $PD1^+$ $CD101^+$ ($TCF1^{low}$) exhausted memory $CD8^+$ T cells(*43*) did not change (Fig S6B). Finally, within $NKG2A^+$ $CD8^+$ NK cells, there was a pronounced increase in CD16 expression and an initial increase in the proliferation marker Ki67 (AC1 vs BC1; Fig 4F).

High-dimensional data visualization with tSNE and clustering analysis with FlowSOM(*44*) confirmed the results of the classical analysis. We performed tSNE and FlowSOM after data clean up with FlowClean and normalization with the SwiftReg algorithm(*45*). The analysis was performed on before (BC1) and after the last cycle (AC4) only (Fig 4G and Fig S7A) and on all

time points analyzed (Fig S7B and S7C). When we compared only BC1 and AC4, the PhenoGraph clustering algorithm identified 36 populations. FlowSOM with 36 populations identified 6 populations of $CD4^+$ T cells, 6 of $CD8^+$ T cells and 4 of NK cells ($NKG2A^{high}$ $CD8^+$; Fig S7A). The remaining populations were likely monocytes and other minor subsets. Direct comparison of each population revealed a decrease in Pop 31 (naïve CD8 T cells) and Pop 30 (central memory $Ki67^+$ $CD8^+$ T cells) and an increase in Pop 2 and 3 (effector and central memory $CD4^+$ T cells). Finally, there was a decrease in HLA-DR high Pop0 and an increase in $CD16^{high}$ $NKG2A^-$ Pop14 (Fig 4H and S7A). Visual inspection of the tSNE plots (Fig 4G) revealed 3 areas mostly occupied by cells in the post-galunisertib AC4 group (New1, 2 and 3) which were characterized by high levels of CD16 and GRZB (New 3 is likely NK cells). In contrast, 3 areas mostly occupied by cells in the pre-galunisertib group BC1 (Old1, 2 and 3) were characterized by high levels of TCF1 and low CD95, confirming the finding of the classical analysis. Analysis of all time points with phenograph-derived 38 populations in FlowSOM recapitulated findings obtained with the classical analysis and the BC1 AC4 comparison with no additional insights (Fig 4I).

Galunisertib treatment in vivo increases pTreg while decreasing pTfh

The frequencies of circulating Tregs and Tfh cells were monitored with an established flow cytometry panel(*46, 47*) after the first and third cycle of galunisertib. The frequency of all $CD4^+$ Tregs ($CD25^{high}$ $FoxP3^+$; gating in Fig S8) and $CD8^+$ Tregs increased after the first cycle and remained higher until the end of the 3rd cycle, while $CCR4^+$ Treg were proportionally higher at the end of the treatment compared to before (Fig 4J). In contrast, circulating Tfh ($CXCR5^+$ $PD1^+$; gating in Fig S8) were lower at the end of the Galunisertib treatment both within total and central memory $CD4^+$ T cells (Fig 4J). Finally, the expression of CD39 (ecto-nucleotide triphosphate

diphosphohydrolase 1), which tracks within extracellular adenosine and immunosuppressive effects, was lower on total and central memory $CD4^+$ T cells (Table S5 and Fig 4J, respectively).

Bulk RNAseq of PBMC and single-cell (sc)RNAseq analysis of LN confirm a profound shift toward effector phenotype.

In our previous studies, we determined that 6hrs after galunisertib treatment in naïve macaques there was an upregulation of the AP1 complex (JUN and FOS) and several genes encoding ribosomal proteins in $CD4^+$ T cells(*42*). To understand early and later effect of galunisertib in the context of SIV infection, in the current study we performed bulk RNAseq of PBMC isolated 1hr after the first administration of galunisertib in cycle 1 and at the end of the 1st 2-weeks cycle. We found 640 genes significantly modulated (FDR q<0.05; $log_2FC=2$) in PBMC just 1hr after the first dose of galunisertib. The majority (457 genes) were downregulated (Fig 5A). Gene set enrichment analysis (GSEA) revealed an upregulation of the oxidative phosphorylation (OXPHOS; ES 0.58 FDR q=0.048)) and the reactive oxygen (ES 0.55 FDR q=0.075) pathways among the Hallmark genet sets (Fig 5A and S9). Among the Biocarta sets, there was an enrichment in the electron transport chain (ETC; ES 0.84 FDR q=0.132) and a downregulation of the circadian (ES -0.81 FDR q=0.163) pathways (Fig 5A and S9). Finally, among the top modulated genes there were several genes encoding for soluble transporters, while classical activation markers like CD69 and CD38 were downregulated (Fig S9B). An early engagement of metabolic pathways was confirmed by enrichment analysis of significant DEG with Metascape(*48*) with an upregulation of adipogenesis, OXPHOS and fatty acid metabolism (Fig S9C). Of note, 2 weeks after the beginning of galunisertib, metabolic pathways were still among the most enriched upregulated pathways in PBMCs (Fig 5B and Fig S10A). Among the top upregulated genes there were CD44, CCR5, several integrins and GRZA and GRZB (Fig S10B). Finally, we performed bulk RNAseq of rectal biopsy tissue before and after the first cycle with

galunisertib (Fig 5C). There were only 51 differentially expressed genes (DEGs; Adjp<0.05; $log_2FC=2$). GSEA analysis of all DEGs (Adjp<0.05) revealed the G2_M_DNA replication pathway highly enriched (ES 0.97 FDR q=0.012) within the Hallmark set. Among the most interesting changes, we observed a pronounced downregulation of integrin β7, in contrast to an increase in integrin αE (CD103; Fig 6C), suggesting that TGF-β-driven increase in αE(*49*) may be driven by non-canonical TGF-β pathway signaling not blocked by galunisertib.

To clarify the impact of galunisertib at the single cell level and in lymphoid tissues, we also performed scRNAseq analysis of cells isolated from LNs before (right axillar) and after (right or left inguinal) the first cycle (Fig 6). Dimensionality reduction and clustering analysis with PCA and uniform manifold approximation and projection (UMAP)(*50*) was performed to visualize the data (Fig 6A). However, cells were classified based only on gene expression (Fig 6B and C). We first classified major subsets: T cells (38,705 cells), B cells (31,385 cells), NK cells (1,628 cells), macrophages (285) and cells expressing both CD19 and CD3 (942 T/B cells) (Fig 6A shows this classification over UMAP). Then we classified only $CD4^+$ and $CD8^+$ T cell subsets (Fig 6C and S11A) and B/T subsets including naïve and germinal center (GC) B cells and Tfh cells (Fig S11B and S11C). Cell number for all these subsets did not change with treatment (Fig S12). However, differential gene expression analysis of T cells revealed an upregulation of members of the AP1 complex, CD69, β2 macroglobulin and RPL13 among the most upregulated genes (Fig 6D). Moreover, it confirmed a downregulation of TCF1 at the transcriptional level (TCF7 gene; Fig 6D). Gene enrichment analysis revealed again Myc_targets_V1, OXPHOS and mTORC1 as the most enriched hallmark pathways (Fig 6E). Of note, among gene ontology cellular processes, RNA processing was the most highly enriched pathway with intracellular transport and catabolic processes following right after (Fig S13A) confirming an increase in translation and metabolism within these cells.

Since we noticed substantial differences in the impact of galunisertib on $CD4^+$ T cells compared to $CD8^+$ T cells by flow, we focused the analysis on these subsets. In $CD4^+$ T cells we found only 25 DEGs with a $log_2FC=0.15$, while 34 DEGs were in $CD8^+$ T cells with more downregulated genes in the $CD8^+$ T cells compared to the $CD4^+$ T cells. The AP1 complex and TCF7 were again upregulated and downregulated respectively in both $CD4^+$ (Fig 6F) and $CD8^+$ T cells (Fig 6G). However, STAT1 was more strongly downregulated in $CD4^+$ T cells. Enrichment analysis showed once again upregulation of Myc_targets_V1, OXPHOS and mTORC1 pathways in both $CD4^+$ and $CD8^+$ T cells (Fig 6H and Fig S13B). Interestingly, the most enriched set among in Biocarta was the HIV-Nef pathway (Fig 6J) demonstrating the relevance of these galunisertib-driven changes to HIV cell cycle and transcription (highly enriched KREB pathway as well). The 2nd most enriched Biocarta pathway was TCR signaling, linking galunisertib to cell activation. Next, we analyzed changes in gene expression in Tfh cells. In this subset we obtained a similar number of DEG as in other T cells and myc_targets_V1 was still the most enriched hallmark pathway (Fig S13C and D). In B cells, the AP1 complex was again prominently upregulated, together with CD83, CD69 and MAMU-DR. Of note, more genes were modulated in B cells (44 genes with a $log_2FC=0.15$ and 18 with logFC0.2) than in T cells with some differences in enriched pathways (Fig S13F). Similar genes were modulated in GC B cells and naïve B cells with several more DEGs in naïve B cells than in GC cells (Fig S14A and B). Finally, 144 genes were modulated in NK cells and 39 genes in macrophages (Fig S14C and D; $log_2FC=0.15$). GRZB was prominently upregulated, but CD44 downregulated. In macrophages genes were mostly downregulated including TCF7L2 and KLF4 suggesting an increase in inflammatory phenotype and decrease in M2 polarization(*51*) (Fig S14D).

Galunisertib increases SIV-specific responses and changes barcode distribution

In order to understand how galunisertib affected immune cell function and SIV-specific responses, we stimulated PBMC with 15-mer SIV peptides from SIVmac239 gag, pol and env

for 24hrs on antibody coated Elispot plates. Because of sample availability, we probed before and after the first cycle and after the 3rd galunisertib cycle only. Interestingly, by the end of the 3rd cycle there was a significant increase in IFN-γ secretion both SIV-specific (particularly against env) and non-specific (DMSO control). TNF-α release increased particularly in response to Gag and non-specifically (Fig 7). However, IL-2 release appeared to increase slightly after the first cycle (non-significant), but remained unchanged with a slight decrease by the end of the 3rd cycle (Fig 7).

In order to understand if these changes in immune responses in combination with latency reversal and switch toward an effector phenotype may have impacted viral population dynamics, we analyzed changes in numbers and distribution of the viral barcodes before and after the first 3 treatment cycles. There was no barcode amplification at several time points particularly in the lymph nodes. However, although there were no significant changes in the number or diversity (measured as Shannon Entropy; Sh) of barcodes before and after each galunisertib cycle (Fig S15A and Fig 8A), we found significant changes in barcode frequency distribution in most tissues and cycles after galunisertib treatment (Fig 8B and S15B). Specifically, the relative proportion of each barcode changed in all monkeys in all cycles in the rectal biopsies (probably a consequence of different sampling area), but also for all LN analyzed (except for 08M134 in cycle 1). Of note, the same LN were sampled at the beginning and after cycle 3 (Table S6). Hence, sampling location does not explain the changes barcode distribution. Changes in the proportion of barcodes were also detected in at least half of the PBMCs after cycle 1 and 2 (cycle 3 not analyzed). Finally, barcode diversity decreased in plasma post-ATI compared to the time point right before ART (Fig 8C) and barcode distribution significantly changed post-ATI compared to pre-ART in 2 of the 7 macaques that rebounded (Fig S15C).

TCF1 downregulation in CD4$^+$ T cells correlates with virological and immunological endpoints.

In order to explore a possible association between the various virological and immunological parameters and their changes, we built a correlation matrix with a curated set of variables of interest or their fold changes. This analysis revealed an association between the decrease in TCF1 expression in the CD4$^+$ T cells and several virological and immunological variables (Fig 8E). Specifically, both the levels of CA-vDNA in the colorectal tissue and the fold increase in gut-SUV strongly inversely correlated with fold changes in TCF1. Since TCF1 decreased, a larger decrease in TCF1 was directly proportional to residual vDNA in the gut at the end of cycle 4 and to the increase in PET signal in the gut (Fig 8D and 8E). A weaker, but still significant association was also present with CA-vDNA in PBMC at the end of cycle 3 and with the levels of vRNA in the lymph nodes at the end of the 4th cycle (Fig 8D and S16A). Finally, the decrease in TCF1 correlated with the increase in IFN-γ and poly-functional IFN-γ/TNF-α releasing cells (cumulative increase of SIV-specific responses to gag, pol and env; Fig 8D and 8E). Of note, the increase in PET signal in the gut also correlated with the levels of vDNA in PBMC at the end of cycle 3, vDNA in gut biopsies and residual CA-vRNA in LN at the end of cycle 4 (Fig S16B). Interestingly, the levels of residual CA-vRNA in LN also correlated with the increase in IFN-γ and poly-functional IFN-γ/TNF-α releasing cells (Pearson r=0.85 and 0.76, respectively). Finally, the residual intact pro-virus (IPDA) directly correlated with the levels of IFN-γ and IFN-γ/TNF-α produced in response to SIV peptides at the end of cycle 3 (Fig 8D; r= 0.76 and 0.88, respectively). In contrast, the change in intact provirus trented to correlate inversely with the levels of IFN-γ, so that a larger decrease directly correlated with more IFN–γ responses. However, this did not reach significance (p=0.117, Fig S16C).

Discussion

HIV-1 latency in T cells is maintained through diverse mechanisms that include blocks in transcriptional elongation, completion, and splicing(*13*). A common characteristic shared by HIV-1 latently infected cells of both T and myeloid cell lineages is their “resting” phenotype(*14, 52-54*) In these cells, an inability to transcribe proviral DNA is linked to a generalized decrease in transcriptional activity which, in turn, is linked to their metabolic status(*23*). Cellular metabolism is in turn influenced by tissue location and environmental cues(*55*).

TGF-β is released at high level in PLWH and its levels remain high during ART(*56*). The immunosuppressive activity of TGF-β is well-known. However, the effect of TGF-β signaling in immune cells is highly context dependent(*57*). Hence, TGF-β plays different roles according to a cell differentiation and activation status(*57*). In $CD8^+$ T cells and NK cells, TGF-β was shown to decrease mTOR activity and preserve cellular metabolism (high mitochondrial activity and spare respiratory capacity, but reduced mTOR activity) preventing metabolic exhaustion(*25, 26, 58, 59*). This effect was linked to survival of antigen-specific $CD8^+$ T cells, preservation of their stemness and it was linked to higher expression of the TCF1 factor(*25*).

In contrast, in $CD4^+$ T cells TGF-β is known to decrease TCR activation(*29, 60*), restrict proliferation and inhibit cytotoxicity (including granzyme and perforin release) at different stage of infection in vivo(*30, 61*). However, the role of TGF-β in the formation and preservation of $CD4^+$ T cell memory is still unclear(*57*). Moreover, the link between TGF-β signaling and TCF1 expression in $CD4^+$ T cells is unexplored.

Here, we used a clinical stage small drug, galunisertib, developed by Eli Lilly and used in several phase 1 and 1/2 clinical studies against solid cancer(*39, 62, 63*) to investigate the impact of TGF-β blockade on SIV latency, SIV reservoir and immune responses. Of note, Eli Lilly did not terminate galunisertib development program because of toxicity(*64, 65*). Indeed, in our studies in macaques, we observed no adverse events nor changes in chemical or hematological variables. Moreover, there were no detectable changes in the levels of the 24

inflammatory factors that we probed in plasma during the treatment. This suggests that this therapeutic approach may be safe in people living with HIV (PLWH).

The first important finding of our study was the confirmation of our previous report of the latency reversal properties of TGF-β blockade in vivo(*35*). Indeed, we found increase in pVL in 7 out of the 8 macaques upon initiation of galunisertib therapy. Although not all macaques were fully suppressed before treatment, substantial increases in pVL (>10^2 copies/ml) were noted also in fully suppressed macaques (08M171, A8R095 and A8L057). Moreover, extensive viral reactivation was documented in tissues by immunoPET/CT. The increase detected post-galunisertib in gut SUV correlated with CA-vRNA as in our previous studies(*35*) and, interestingly, it was associated with a decrease in TCF1. Galunisertib led to increased probe uptake in the gut and lymphoid tissues, as well as a generalized increase in whole-body uptake. Yet, there was no change in the PET background signal in kidneys and spleen. This, in conjunction with our previous studies demonstrating the specificity of the PET signal for areas of enhanced SIV replication in gut and lymph nodes(*35, 41, 66*), demonstrates that the galunisertib-driven increases in SUV were mostly specific, and highlighted areas of SIV latency reversal at least in gut and lymphoid tissues. The extent to which the increased signal in the spine and bones recapitulates an increase in SIV replication at these sites remains to be determined.

Importantly, we observed a decrease in CA-vDNA in all the tissues that cannot be attributed to ART alone. Indeed, although we did not have a concurrent control group, this decrease was not present in similar studies conducted in SIVmac239M2 infected macaques on the same ART regimen, but not treated with galunisertib. Considering studies by other groups with different models (SIVmac251), they report 2nd phase decay of SIV intact provirus (weeks ~32 to ~100pi, Fig 2B in(*67*)) with a $t_{1/2}$ of >8 months(*67*). In contrast, in our study, the intact provirus decreased by 3 folds (median) in a little over 3 months (from week 35pi, BC1 to week 49pi, AC4). Interestingly, this decrease in intact pro-virus trended toward a direct correlation with IFN-γ

responses. However, IFN–γ levels also inversely correlated with the absolute value of residual intact provirus, suggesting that IFN-γ responses were driven by residual viral reservoir while, at the same time, were involved in clearing intact virus. Indeed, the increase in IFN-γ and TNF-α also correlated with residual CA-vRNA in the LN at the end of the treatment. The latter, in turn, was directly proportional to the increase in gut SUV. This is in line with increased latency reversal explaining residual viral RNA in lymphoid tissues.

Finally, one of our most intriguing results was the profound downregulation of TCF1 in $CD4^+$ T cells at both the transcriptional and protein levels. Although TCF1 is conventionally viewed as an effector of the canonical Wnt pathway(*68*) and recently reached notoriety for its role in maintaining stemness of antigen-specific memory $CD8^+$ T cells(*26, 69*), TCF1 has a plethora of functions in T cell development and differentiation largely independent of Wnt signaling(*22*). In $CD4^+$ T cells, TCF1 has been implicated in orchestrating all the major Th subsets, including Th1, Th2, Th17 and Tfh(*70*). TCF1 is known to control the bifurcation between Th1 and Tfh in favor of Tfh cells(*70*), while it negatively regulates Treg development(*22*). This is in line with our findings of increased Treg and decreased Tfh, in the midst of a profound downregulation of TCF1. Importantly, TCF1 is downregulated with increased cellular differentiation and progression toward effector functions in T cells. T cell activation leads to reduced levels of TCF1 and higher levels of TCF1 are present in T cells with higher stemness and low anabolic metabolism(*68*). These findings suggest that TCF1 has a critical role in maintaining quiescence in immune cells likely in concert with TGF-β(*18, 61*). Our data reveal that this link may be even more prominent and important in $CD4^+$ T cells than in $CD8^+$ T cells. Importantly, the decrease in TCF1 was accompanied with enhancement in other effector markers such as CD95, CD16 and GRZB (at the transcriptional level) and an increase in the transcription of AP1 complex. However, there was no clear upregulation of other classical markers of immune activation such as CD69 and no increase in T cell proliferation (Ki67 expression). Hence, galunisertib treatment

does not appear to lead to classical T cell activation. Instead, in vivo TGF-β blockade seems to primarily change the metabolic state of T cells (and likely other immune cells) increasing OXPHOS and mitochondrial function. Of note, although glycolysis is essential during cell activation, mitochondrial pathways are engaged and remodeled early after activation and OXPHOS upregulation has a pivotal role in the earliest stages of cell activation(*18*).

Hence, we propose a model in which TGF-β inhibition forces cells (particularly $CD4^+$ T cells) out of quiescence to a transitional state where they reinitiate their transcriptional program and are metabolically ready to be activated and effector. In absence of direct TCR engagement or other activation stimuli, they do not undergo full/classical activation and proliferation, yet they can reinitiate viral transcription and respond to SIV antigenic stimulation. Indeed, functionally, we demonstrated that the PBMC after galunisertib treatment secrete higher levels of IFN-γ and TNF-α. Interestingly, there was no increase in IL-2 secretion. The link between TGF-β and IL-2(*71*) and the critical role of IL-2 in T cell proliferation again suggest that galunisertib enhances an effector phenotype uncoupled from cellular proliferation. scRNAseq analysis demonstrated a trend toward an effector phenotype also in other immune cells, such as B cells, NKs and macrophages. Future studies will need to uncover in depth the effect of TGF-β blockade on these other immune subsets.

This study has several limitations. The most important limitations are the relatively small number of macaques and the lack of a concurrent untreated control group. We also could not investigate in depth the viral kinetics after ART interruption because of the short follow up after ATI. Moreover, we did not explore changes in the phenotype or turnover of cells isolated from gut and lymph nodes and relied solely on transcriptional data for these tissues. Finally, because of sample availability, we could not dissect the cellular origin of increased IFN-γ and TNF-α.

In conclusion, we report that in vivo treatment with a clinical stage small molecule TGF-β inhibitor drives an effector phenotype in T cells that is likely responsible for increasing the

frequency of spontaneous latency reversal events, stimulating SIV-specific immune responses, and decreasing the viral reservoir. Future work will determine whether the galunisertib-driven enhanced antiviral responses and decreased viral reservoirs can significantly contribute to post-ART virological control.

MATERIALS AND METHODS

Study design and Ethics Statement

A total of 8 adult female Indian origin *Rhesus* macaques (*Macaca mulatta*; Mamu A*01, B*08 and B*17 negative) were used for the study described in the manuscript (Table S1). All the macaques were selected form the colonies bred and raised at the New Iberia Research Center (NIRC), University of Louisiana at Lafayette. Treatments were in accordance with NIRC standards which comply with the Guide for the Use and Care of Laboratory Animals. Any abnormal observations and/or signs of illness or distress were reported per NIRC SOPs. Appropriate procedures were performed to ensure that potential distress, pain, discomfort were limited to that unavoidable in the conduct of the research plan. Ketamine (10mg/kg) and/or telazol (4mg/kg) sedation were used for sample administration, collection of samples and conducting image collections. Analgesics were used when determined appropriate by veterinary medical staff. Monkeys were fed Teklad monkey chow supplemented with fresh fruit or vegetables and water ad libitum.

Rhesus macaques (n=8 main study + 4 separate non-concomitant study) were infected with 300 $TCID_{50}$ of the barcoded SIVmac239M2 stock intravenously and ART (Tenofovir [PMPA], Emtricitabine [FTC] and Dolutegravir [DTG]) was initiated on week 6 pi. Galunisertib treatment was initiated on week 35 p.i. Powder (MedChemExpress – MCE, NJ, USA) was dissolved in water and given orally in a treat twice daily at 20mg/kg. 4 cycles of 2 weeks daily treatment with 2 weeks wash out period were performed. Macaques 08M156 and A6X003 were given the rhesus recombinant antibody (rhesus/human chimeric) anti-PD1 antibody [NIVOR4LALA;

comprising silenced rhesus IgG4k constant regions and variable regions from anti-human PD-1, nivolumab; non-human primates reagents resource, NHPRR.

Blood viral load was monitored biweekly before and during ART and every 3-4 days during Galunisertib treatment. Colorectal biopsies and LN FNA were collected before and after galunisertib treatment. ART was terminated 3 weeks after the last galunisertib dose and euthanasia and necropsy to harvest tissues were performed at week 58 post infection, tissues samples were flash frozen, fixed in OCT or Z-fix.

Plasma and Tissue SIV Viral loads (VL)

Blood was collected in EDTA tubes and plasma was separated by density gradient centrifugation and used for the determination of plasma VL by SIVgag qRT-PCR at NIRC or at Leidos (Quantitative Molecular Diagnostics Core, AIDS and Cancer Virus Program Frederick National Laboratory). Tissue VL from snap frozen PBMC pellets, colorectal biopsies and LN FNA were performed as described in (*72*). SIV-TILDA was performed on freshly stored PBMC before cycle 1 and at the end of cycle 4 of galunisertib by Accelevir, Baltimore, MD.

ImmunoPET/CT

ImmunoPET/CT for mapping SIV signals in total body scans were conducted in part as reported previously(*42*). The probe consisted of primatized p7D3 anti-env F(ab)'2 coupled with the chelator DOTA and labeled with Cu^{64} just prior to administration to the animals. For probe administration, the animals were sedated, and a venous catheter was placed into an arm of leg vein to minimize bleeding of the probe into the tissue surrounding the site of injection. The probe for each animal consisted of ~1mg of the p7D3 F(ab)'2 labeled with 2-3 mCi of ^{64}Cu. After injection, the animals were allowed to recuperate in their cage until the next day. At 24 hours, the animals were again anesthetized with Telazol and the macaque's body was immobilized in

dorsal recumbency on the scanner table. Scans were conducted in a Phillips Gemini TF64 scanner. The final CT image was compiled from 200 to 300 slices, depending on macaque size. PET Image analysis was performed using the MIM software. PET/CT fusions were generated scaled according to calculated Standardized Uptake Values (SUV). The SUV scale for the PET scans was selected based on the overall signal intensity of the PET scans (whole body), and the CT scale was selected for optimal visibility of the tissues. All images and maximum image projections were set to the same scale for visual comparisons. Additional details on MIM analysis are described in Supplemental Methods.

Cell isolation, flow cytometry staining, classical and high-dimensional analysis

Colorectal biopsy tissues were isolated by enzymatic digestion while LN biopsies were passed through a 70µm cell strainer as described in(*42*). Isolated cells were phenotyped with panels listed in Supplemental Table S4. FlowJo vs 10.8 was use for both classical and high-dimesional analysis. PeacoQC, FlowtSNE and FlowSOM plug-ins were used with default settings. SwiftReg was used for normalization(*45*). More details on the staining procedures and analysis pipeline in Supplemental Methods.

Bulk and scRNAseq analysis

For bulk RNAseq, snap frozen PBMC pellets from BC1, 1hr after first Gal dose and AC1 were used for RNA extraction with the RNeasy kit with on column DNA digestion (Qiagen). Library preparation was performed using TruSeq Stranded Total RNA with Ribo-Zero Globin and sequencing was done with an Illumina HiSeq4000 with >20M reads/samples. Sequencing data was demultiplexed and trimmed using Trimmomatic v0.36 to remove adapters and low-quality reads. Trimmed reads were aligned to the Mmul10 reference genome and transcripts quantified using the Hisat2-StringTie pipeline(*73*). Differential gene expression analysis using the quantified gene transcripts was performed with DESeq2 R package(*74*) comparing the samples

attained before and after galunisertib treatment and controlling for intra-animal autocorrelation. Differentially expressed genes (DEGs) were analyzed by functional enrichment analysis and gene set enrichment analysis (GSEA) to identify specific pathways and molecular processes altered by galunisertib.

The Parse pipeline and Partek software were. For bulk RNAseq features with <100 counts were removed, data normalized and DESeq2 was used to obtain a DEG list. Genes with a false discovery rate (FDR)-adjusted p-value ≤0.05 and absolute $\log_2$ fold-change (FC) (compared to BC1) above 2 were defined as significantly differentially expressed (DEG). For scRNAseq analysis cells isolated from lymph nodes before (BC1) and after (AC1) galuniertib were fixes with the Parse fixation kit, barcoded and sequenced at the NUseq Core. The Partek software was used for scRNAseq analysis. Cells with 400-8000 features, excluding features with 0 reads in >99.99 cells, were included. Scran deconvolution was used for normalization and cell classification was based on gene expression. Hurdle models were used to compare DEGs in each cell subset before and after galunisertib. See supplemental methods for a detailed description of scRNAseq analysis and additional control analysis using Seurat R package with more stringent QC cut-offs and SCTransform normalization.

Plasma cytokines and T cell responses

Cytokines in plasma (at 1:2 dilution) were measured using the NHP Cytokine 24-Plex kit by Meso Scale Diagnostics (MSD) according to manufacturer instructions. Frozen PBMC collected at week 6 post-infection (pre-ART), right before the first galunisertib administration (BC1), at the end of cycle 1 (AC1) and at the end of cycle 3 (AC3) were thawed in AIM V medium (Thermo Fisher) with benzonase (Sigma) and plated on a FluoroSpot (CTL) plate pre-activated with 70% Ethanol and IFN-γ, TNF-α and IL-2 capture solution. Gag, pol, and env 15-mer peptides (NIH AIDS Reagents program) were prepared at two times the final concentration of 2.5µg/ml with co-stimulatory reagents anti-CD28 10µg/ml and anti-CD49d 10µg/ml and added to the cells in

CTL-Test™ Medium. Parallel positive control of PMA (20ng/mL) and ionomycin (200ng/mL) or mock DMSO solution was also plated with the stimulatory reagents. PBMCs were added at 300,000 cells per well. After 24hrs, the plate was washed, and incubated with detection and tertiary solutions and shipped to CTL for scanning and QC.

Statistics

GraphPad Prism v10, R and Python were used for statistical analysis and data visualization. Wilcoxon matched-pairs test and repeated measures ANOVA or mixed effect analysis (when the data set had missing data) were used to compare the different virological and immunological variables between baseline (BC1) and a single or multiple post-galunisertib time points. In Prism the mixed model uses a compound symmetry covariance matrix, and is fit using Restricted Maximum Likelihood (REML). Cytokine data from MSD assay were first Log transformed, then normalized by subcolumn/factor in percentage with 0% as smallest value and 100% larger value in each dataset. Each factor was analyzed separately with ANOVA for repeated measures and Dunn's multiple comparison's post-hoc test and together by principal component analysis (PCA). Holm-Sidak test was used for multiple comparison correction in all cases, but FlowSOM cluster comparison where the FDR method was used. Pearson r coefficient was calculated for pairwise tests of association in a correlation matrix with selected variables. For RNAseq analysis see above and supplemental methods. For viral population analysis, Shannon Entropy of the viral barcodes present in each sample was used to measure the diversity of the viral populations (see supplemental Methods). Chi-squared tests were used in R to compare barcode composition between before and after cycle time points within a tissue/macaque using paired barcode relative frequencies. Unless otherwise specified p-value<0.05 was considered statistically significant.

LIST OF SUPPLEMENTARY MATERIALS

Supplementary Methods

Supplementary Figure Fig. S1 to S16

Supplementary Table S1 to S6

Movies S1 to S8

REFERENCES

1. P. Gantner, S. Buranapraditkun, A. Pagliuzza, C. Dufour, M. Pardons, J. L. Mitchell, E. Kroon, C. Sacdalan, N. Tulmethakaan, S. Pinyakorn, M. L. Robb, N. Phanuphak, J. Ananworanich, D. Hsu, S. Vasan, L. Trautmann, R. Fromentin, N. Chomont, HIV rapidly targets a diverse pool of CD4(+) T cells to establish productive and latent infections. *Immunity* **56**, 653-668 e655 (2023).
2. J. B. Whitney, A. L. Hill, S. Sanisetty, P. Penaloza-MacMaster, J. Liu, M. Shetty, L. Parenteau, C. Cabral, J. Shields, S. Blackmore, J. Y. Smith, A. L. Brinkman, L. E. Peter, S. I. Mathew, K. M. Smith, E. N. Borducchi, D. I. Rosenbloom, M. G. Lewis, J. Hattersley, B. Li, J. Hesselgesser, R. Geleziunas, M. L. Robb, J. H. Kim, N. L. Michael, D. H. Barouch, Rapid seeding of the viral reservoir prior to SIV viraemia in rhesus monkeys. *Nature* **512**, 74-77 (2014).
3. D. Persaud, Y. Zhou, J. M. Siliciano, R. F. Siliciano, Latency in human immunodeficiency virus type 1 infection: no easy answers. *J Virol* **77**, 1659-1665 (2003).
4. D. M. Margolis, N. M. Archin, Proviral Latency, Persistent Human Immunodeficiency Virus Infection, and the Development of Latency Reversing Agents. *The Journal of infectious diseases* **215**, S111-S118 (2017).
5. T. A. Wagner, S. McLaughlin, K. Garg, C. Y. Cheung, B. B. Larsen, S. Styrchak, H. C. Huang, P. T. Edlefsen, J. I. Mullins, L. M. Frenkel, HIV latency. Proliferation of cells with HIV integrated into cancer genes contributes to persistent infection. *Science* **345**, 570-573 (2014).
6. F. Maldarelli, X. Wu, L. Su, F. R. Simonetti, W. Shao, S. Hill, J. Spindler, A. L. Ferris, J. W. Mellors, M. F. Kearney, J. M. Coffin, S. H. Hughes, HIV latency. Specific HIV integration sites are linked to clonal expansion and persistence of infected cells. *Science* **345**, 179-183 (2014).
7. L. B. Cohn, I. T. Silva, T. Y. Oliveira, R. A. Rosales, E. H. Parrish, G. H. Learn, B. H. Hahn, J. L. Czartoski, M. J. McElrath, C. Lehmann, F. Klein, M. Caskey, B. D. Walker, J. D. Siliciano, R. F. Siliciano, M. Jankovic, M. C. Nussenzweig, HIV-1 integration landscape during latent and active infection. *Cell* **160**, 420-432 (2015).
8. K. B. Einkauf, M. R. Osborn, C. Gao, W. Sun, X. Sun, X. Lian, E. M. Parsons, G. T. Gladkov, K. W. Seiger, J. E. Blackmer, C. Jiang, S. A. Yukl, E. S. Rosenberg, X. G. Yu, M. Lichterfeld,

650 Parallel analysis of transcription, integration, and sequence of single HIV-1 proviruses.
651 *Cell* **185**, 266-282 e215 (2022).
652 9. X. Lian, K. W. Seiger, E. M. Parsons, C. Gao, W. Sun, G. T. Gladkov, I. C. Roseto, K. B.
653 Einkauf, M. R. Osborn, J. M. Chevalier, C. Jiang, J. Blackmer, M. Carrington, E. S.
654 Rosenberg, M. M. Lederman, D. K. McMahon, R. J. Bosch, J. M. Jacobson, R. T. Gandhi,
655 M. J. Peluso, T. W. Chun, S. G. Deeks, X. G. Yu, M. Lichterfeld, Progressive transformation
656 of the HIV-1 reservoir cell profile over two decades of antiviral therapy. *Cell Host*
657 *Microbe* **31**, 83-96 e85 (2023).
658 10. V. Singh, A. Dashti, M. Mavigner, A. Chahroudi, Latency Reversal 2.0: Giving the Immune
659 System a Seat at the Table. *Curr HIV/AIDS Rep* **18**, 117-127 (2021).
660 11. E. Abner, A. Jordan, HIV "shock and kill" therapy: In need of revision. *Antiviral Res* **166**,
661 19-34 (2019).
662 12. A. Ait-Ammar, A. Kula, G. Darcis, R. Verdikt, S. De Wit, V. Gautier, P. W. G. Mallon, A.
663 Marcello, O. Rohr, C. Van Lint, Current Status of Latency Reversing Agents Facing the
664 Heterogeneity of HIV-1 Cellular and Tissue Reservoirs. *Frontiers in microbiology* **10**, 3060
665 (2019).
666 13. S. A. Yukl, P. Kaiser, P. Kim, S. Telwatte, S. K. Joshi, M. Vu, H. Lampiris, J. K. Wong, HIV
667 latency in isolated patient CD4(+) T cells may be due to blocks in HIV transcriptional
668 elongation, completion, and splicing. *Sci Transl Med* **10**, (2018).
669 14. J. D. Siliciano, R. F. Siliciano, Low Inducibility of Latent Human Immunodeficiency Virus
670 Type 1 Proviruses as a Major Barrier to Cure. *J Infect Dis* **223**, 13-21 (2021).
671 15. Y. C. Ho, L. Shan, N. N. Hosmane, J. Wang, S. B. Laskey, D. I. Rosenbloom, J. Lai, J. N.
672 Blankson, J. D. Siliciano, R. F. Siliciano, Replication-competent noninduced proviruses in
673 the latent reservoir increase barrier to HIV-1 cure. *Cell* **155**, 540-551 (2013).
674 16. E. N. Borducchi, C. Cabral, K. E. Stephenson, J. Liu, P. Abbink, D. Ng'ang'a, J. P. Nkolola, A.
675 L. Brinkman, L. Peter, B. C. Lee, J. Jimenez, D. Jetton, J. Mondesir, S. Mojta, A.
676 Chandrashekar, K. Molloy, G. Alter, J. M. Gerold, A. L. Hill, M. G. Lewis, M. G. Pau, H.
677 Schuitemaker, J. Hesselgesser, R. Geleziunas, J. H. Kim, M. L. Robb, N. L. Michael, D. H.
678 Barouch, Ad26/MVA therapeutic vaccination with TLR7 stimulation in SIV-infected
679 rhesus monkeys. *Nature* **540**, 284-287 (2016).
680 17. C. C. Nixon, M. Mavigner, G. C. Sampey, A. D. Brooks, R. A. Spagnuolo, D. M. Irlbeck, C.
681 Mattingly, P. T. Ho, N. Schoof, C. G. Cammon, G. K. Tharp, M. Kanke, Z. Wang, R. A. Cleary,
682 A. A. Upadhyay, C. De, S. R. Wills, S. D. Falcinelli, C. Galardi, H. Walum, N. J. Schramm, J.
683 Deutsch, J. D. Lifson, C. M. Fennessey, B. F. Keele, S. Jean, S. Maguire, B. Liao, E. P.
684 Browne, R. G. Ferris, J. H. Brehm, D. Favre, T. H. Vanderford, S. E. Bosinger, C. D. Jones, J.
685 P. Routy, N. M. Archin, D. M. Margolis, A. Wahl, R. M. Dunham, G. Silvestri, A. Chahroudi,
686 J. V. Garcia, Systemic HIV and SIV latency reversal via non-canonical NF-kappaB signalling
687 in vivo. *Nature* **578**, 160-165 (2020).
688 18. D. O'Sullivan, The metabolic spectrum of memory T cells. *Immunol Cell Biol* **97**, 636-646
689 (2019).
690 19. J. M. Crater, D. F. Nixon, R. L. Furler O'Brien, HIV-1 replication and latency are balanced
691 by mTOR-driven cell metabolism. *Front Cell Infect Microbiol* **12**, 1068436 (2022).
692 20. E. Besnard, S. Hakre, M. Kampmann, H. W. Lim, N. N. Hosmane, A. Martin, M. C. Bassik,
693 E. Verschueren, E. Battivelli, J. Chan, J. P. Svensson, A. Gramatica, R. J. Conrad, M. Ott, W.

694 C. Greene, N. J. Krogan, R. F. Siliciano, J. S. Weissman, E. Verdin, The mTOR Complex
695 Controls HIV Latency. *Cell Host Microbe* **20**, 785-797 (2016).
696 21. H. J. Barbian, M. S. Seaton, S. D. Narasipura, J. Wallace, R. Rajan, B. E. Sha, L. Al-Harthi,
697 beta-catenin regulates HIV latency and modulates HIV reactivation. *PLoS Pathog* **18**,
698 e1010354 (2022).
699 22. F. Gounari, K. Khazaie, TCF-1: a maverick in T cell development and function. *Nat*
700 *Immunol* **23**, 671-678 (2022).
701 23. J. C. Valle-Casuso, M. Angin, S. Volant, C. Passaes, V. Monceaux, A. Mikhailova, K.
702 Bourdic, V. Avettand-Fenoel, F. Boufassa, M. Sitbon, O. Lambotte, M. I. Thoulouze, M.
703 Muller-Trutwin, N. Chomont, A. Saez-Cirion, Cellular Metabolism Is a Major Determinant
704 of HIV-1 Reservoir Seeding in CD4(+) T Cells and Offers an Opportunity to Tackle
705 Infection. *Cell Metab* **29**, 611-626 e615 (2019).
706 24. S. A. Oh, M. O. Li, TGF-beta: guardian of T cell function. *Journal of immunology* **191**,
707 3973-3979 (2013).
708 25. S. S. Gabriel, C. Tsui, D. Chisanga, F. Weber, M. Llano-Leon, P. M. Gubser, L. Bartholin, F.
709 Souza-Fonseca-Guimaraes, N. D. Huntington, W. Shi, D. T. Utzschneider, A. Kallies,
710 Transforming growth factor-beta-regulated mTOR activity preserves cellular metabolism
711 to maintain long-term T cell responses in chronic infection. *Immunity* **54**, 1698-1714
712 e1695 (2021).
713 26. Y. Hu, W. H. Hudson, H. T. Kissick, C. B. Medina, A. P. Baptista, C. Ma, W. Liao, R. N.
714 Germain, S. J. Turley, N. Zhang, R. Ahmed, TGF-beta regulates the stem-like state of PD-
715 1+ TCF-1+ virus-specific CD8 T cells during chronic infection. *J Exp Med* **219**, (2022).
716 27. C. Ma, N. Zhang, Transforming growth factor-beta signaling is constantly shaping
717 memory T-cell population. *Proc Natl Acad Sci U S A* **112**, 11013-11017 (2015).
718 28. S. Viel, A. Marcais, F. S. Guimaraes, R. Loftus, J. Rabilloud, M. Grau, S. Degouve, S.
719 Djebali, A. Sanlaville, E. Charrier, J. Bienvenu, J. C. Marie, C. Caux, J. Marvel, L. Town, N.
720 D. Huntington, L. Bartholin, D. Finlay, M. J. Smyth, T. Walzer, TGF-beta inhibits the
721 activation and functions of NK cells by repressing the mTOR pathway. *Sci Signal* **9**, ra19
722 (2016).
723 29. J. S. Delisle, M. Giroux, G. Boucher, J. R. Landry, M. P. Hardy, S. Lemieux, R. G. Jones, B. T.
724 Wilhelm, C. Perreault, The TGF-beta-Smad3 pathway inhibits CD28-dependent cell
725 growth and proliferation of CD4 T cells. *Genes Immun* **14**, 115-126 (2013).
726 30. G. M. Lewis, E. J. Wehrens, L. Labarta-Bajo, H. Streeck, E. I. Zuniga, TGF-beta receptor
727 maintains CD4 T helper cell identity during chronic viral infections. *J Clin Invest* **126**,
728 3799-3813 (2016).
729 31. A. P. Nath, A. Braun, S. C. Ritchie, F. R. Carbone, L. K. Mackay, T. Gebhardt, M. Inouye,
730 Comparative analysis reveals a role for TGF-beta in shaping the residency-related
731 transcriptional signature in tissue-resident memory CD8+ T cells. *PLoS One* **14**, e0210495
732 (2019).
733 32. N. Zhang, M. J. Bevan, Transforming growth factor-beta signaling controls the formation
734 and maintenance of gut-resident memory T cells by regulating migration and retention.
735 *Immunity* **39**, 687-696 (2013).
736 33. T. Hirai, Y. Yang, Y. Zenke, H. Li, V. K. Chaudhri, J. S. De La Cruz Diaz, P. Y. Zhou, B. A.
737 Nguyen, L. Bartholin, C. J. Workman, D. W. Griggs, D. A. A. Vignali, H. Singh, D. Masopust,

738 D. H. Kaplan, Competition for Active TGFbeta Cytokine Allows for Selective Retention of
739 Antigen-Specific Tissue- Resident Memory T Cells in the Epidermal Niche. *Immunity* **54**,
740 84-98 e85 (2021).
741 34. C. Larson, B. Oronsky, C. A. Carter, A. Oronsky, S. J. Knox, D. Sher, T. R. Reid, TGF-beta: a
742 master immune regulator. *Expert Opin Ther Targets* **24**, 427-438 (2020).
743 35. S. Samer, Y. Thomas, M. Arainga, C. Carter, L. M. Shirreff, M. S. Arif, J. M. Avita, I. Frank,
744 M. D. McRaven, C. T. Thuruthiyil, V. B. Heybeli, M. R. Anderson, B. Owen, A. Gaisin, D.
745 Bose, L. M. Simons, J. F. Hultquist, J. Arthos, C. Cicala, I. Sereti, P. J. Santangelo, R.
746 Lorenzo-Redondo, T. J. Hope, F. J. Villinger, E. Martinelli, Blockade of TGF-beta signaling
747 reactivates HIV-1/SIV reservoirs and immune responses in vivo. *JCI Insight* **7**, (2022).
748 36. S. Bergstresser, D. A. Kulpa, TGF-beta Signaling Supports HIV Latency in a Memory CD4+
749 T Cell Based In Vitro Model. *Methods Mol Biol* **2407**, 69-79 (2022).
750 37. S. Chinnapaiyan, R. K. Dutta, M. Nair, H. S. Chand, I. Rahman, H. J. Unwalla, TGF-beta1
751 increases viral burden and promotes HIV-1 latency in primary differentiated human
752 bronchial epithelial cells. *Scientific reports* **9**, 12552 (2019).
753 38. R. B. Holmgaard, D. A. Schaer, Y. Li, S. P. Castaneda, M. Y. Murphy, X. Xu, I. Inigo, J.
754 Dobkin, J. R. Manro, P. W. Iversen, D. Surguladze, G. E. Hall, R. D. Novosiadly, K. A.
755 Benhadji, G. D. Plowman, M. Kalos, K. E. Driscoll, Targeting the TGFbeta pathway with
756 galunisertib, a TGFbetaRI small molecule inhibitor, promotes anti-tumor immunity
757 leading to durable, complete responses, as monotherapy and in combination with
758 checkpoint blockade. *J Immunother Cancer* **6**, 47 (2018).
759 39. D. Melisi, D. Y. Oh, A. Hollebecque, E. Calvo, A. Varghese, E. Borazanci, T. Macarulla, V.
760 Merz, C. Zecchetto, Y. Zhao, I. Gueorguieva, M. Man, L. Gandhi, S. T. Estrem, K. A.
761 Benhadji, M. C. Lanasa, E. Avsar, S. C. Guba, R. Garcia-Carbonero, Safety and activity of
762 the TGFbeta receptor I kinase inhibitor galunisertib plus the anti-PD-L1 antibody
763 durvalumab in metastatic pancreatic cancer. *J Immunother Cancer* **9**, (2021).
764 40. A. Wick, A. Desjardins, C. Suarez, P. Forsyth, I. Gueorguieva, T. Burkholder, A. L. Cleverly,
765 S. T. Estrem, S. Wang, M. M. Lahn, S. C. Guba, D. Capper, J. Rodon, Phase 1b/2a study of
766 galunisertib, a small molecule inhibitor of transforming growth factor-beta receptor I, in
767 combination with standard temozolomide-based radiochemotherapy in patients with
768 newly diagnosed malignant glioma. *Invest New Drugs* **38**, 1570-1579 (2020).
769 41. P. J. Santangelo, K. A. Rogers, C. Zurla, E. L. Blanchard, S. Gumber, K. Strait, F. Connor-
770 Stroud, D. M. Schuster, P. K. Amancha, J. J. Hong, S. N. Byrareddy, J. A. Hoxie, B.
771 Vidakovic, A. A. Ansari, E. Hunter, F. Villinger, Whole-body immunoPET reveals active SIV
772 dynamics in viremic and antiretroviral therapy-treated macaques. *Nat Methods* **12**, 427-
773 432 (2015).
774 42. S. Samer, Y. Thomas, M. Araínga, C. Carter, L. Shirreff, M. Arif, J. Avita, I. Frank, M.
775 McRaven, C. Thuruthiyil, V. Heybeli, M. Anderson, B. Owen, A. Gaisin, D. Bose, L. Simons,
776 J. Hultquist, J. Arthos, C. Cicala, I. Sereti, P. Santangelo, R. Lorenzo-Redondo, T. Hope, F.
777 Villinger, E. Martinelli, Blockade of TGF-β signaling reactivates HIV-1/SIV reservoirs and
778 immune responses in vivo. *bioRxiv*, 2022.2005.2013.489595 (2022).
779 43. S. J. Im, B. T. Konieczny, W. H. Hudson, D. Masopust, R. Ahmed, PD-1+ stemlike CD8 T
780 cells are resident in lymphoid tissues during persistent LCMV infection. *Proc Natl Acad*
781 *Sci U S A* **117**, 4292-4299 (2020).

782 44. S. Van Gassen, B. Callebaut, M. J. Van Helden, B. N. Lambrecht, P. Demeester, T. Dhaene,
783 Y. Saeys, FlowSOM: Using self-organizing maps for visualization and interpretation of
784 cytometry data. *Cytometry A* **87**, 636-645 (2015).
785 45. J. A. Rebhahn, S. A. Quataert, G. Sharma, T. R. Mosmann, SwiftReg cluster registration
786 automatically reduces flow cytometry data variability including batch effects. *Commun*
787 *Biol* **3**, 218 (2020).
788 46. M. J. Blackburn, M. Zhong-Min, F. Caccuri, K. McKinnon, L. Schifanella, Y. Guan, G. Gorini,
789 D. Venzon, C. Fenizia, N. Binello, S. N. Gordon, C. J. Miller, G. Franchini, M. Vaccari,
790 Regulatory and Helper Follicular T Cells and Antibody Avidity to Simian
791 Immunodeficiency Virus Glycoprotein 120. *J Immunol* **195**, 3227-3236 (2015).
792 47. S. Helmold Hait, D. A. Vargas-Inchaustegui, T. Musich, V. Mohanram, I. Tuero, D. J.
793 Venzon, J. Bear, M. Rosati, M. Vaccari, G. Franchini, B. K. Felber, G. N. Pavlakis, M.
794 Robert-Guroff, Early T Follicular Helper Cell Responses and Germinal Center Reactions
795 Are Associated with Viremia Control in Immunized Rhesus Macaques. *J Virol* **93**, (2019).
796 48. Y. Zhou, B. Zhou, L. Pache, M. Chang, A. H. Khodabakhshi, O. Tanaseichuk, C. Benner, S.
797 K. Chanda, Metascape provides a biologist-oriented resource for the analysis of systems-
798 level datasets. *Nat Commun* **10**, 1523 (2019).
799 49. Z. Qiu, T. H. Chu, B. S. Sheridan, TGF-beta: Many Paths to CD103(+) CD8 T Cell Residency.
800 *Cells* **10**, (2021).
801 50. H. S. Lim, P. Qiu, Quantifying Cell-Type-Specific Differences of Single-Cell Datasets Using
802 Uniform Manifold Approximation and Projection for Dimension Reduction and Shapley
803 Additive exPlanations. *J Comput Biol* **30**, 738-750 (2023).
804 51. X. Liao, N. Sharma, F. Kapadia, G. Zhou, Y. Lu, H. Hong, K. Paruchuri, G. H.
805 Mahabeleshwar, E. Dalmas, N. Venteclef, C. A. Flask, J. Kim, B. W. Doreian, K. Q. Lu, K. H.
806 Kaestner, A. Hamik, K. Clement, M. K. Jain, Kruppel-like factor 4 regulates macrophage
807 polarization. *J Clin Invest* **121**, 2736-2749 (2011).
808 52. M. A. Moso, J. L. Anderson, S. Adikari, L. R. Gray, G. Khoury, J. J. Chang, J. C. Jacobson, A.
809 M. Ellett, W. J. Cheng, S. Saleh, J. J. Zaunders, D. F. J. Purcell, P. U. Cameron, M. J.
810 Churchill, S. R. Lewin, H. K. Lu, HIV latency can be established in proliferating and
811 nonproliferating resting CD4+ T cells in vitro: implications for latency reversal. *AIDS* **33**,
812 199-209 (2019).
813 53. J. Neidleman, X. Luo, J. Frouard, G. Xie, F. Hsiao, T. Ma, V. Morcilla, A. Lee, S. Telwatte, R.
814 Thomas, W. Tamaki, B. Wheeler, R. Hoh, M. Somsouk, P. Vohra, J. Milush, K. S. James, N.
815 M. Archin, P. W. Hunt, S. G. Deeks, S. A. Yukl, S. Palmer, W. C. Greene, N. R. Roan,
816 Phenotypic analysis of the unstimulated in vivo HIV CD4 T cell reservoir. *Elife* **9**, (2020).
817 54. A. Chitrakar, M. Sanz, S. B. Maggirwar, N. Soriano-Sarabia, HIV Latency in Myeloid Cells:
818 Challenges for a Cure. *Pathogens* **11**, (2022).
819 55. E. L. Pearce, Metabolism in T cell activation and differentiation. *Curr Opin Immunol* **22**,
820 314-320 (2010).
821 56. H. Valdez, M. M. Lederman, Cytokines and cytokine therapies in HIV infection. *AIDS Clin*
822 *Rev*, 187-228 (1997).
823 57. R. J. Salmond, Regulation of T Cell Activation and Metabolism by Transforming Growth
824 Factor-Beta. *Biology (Basel)* **12**, (2023).

825 58. S. Regis, A. Dondero, F. Caliendo, C. Bottino, R. Castriconi, NK Cell Function Regulation by
826 TGF-beta-Induced Epigenetic Mechanisms. *Front Immunol* **11**, 311 (2020).
827 59. V. Zaiatz-Bittencourt, D. K. Finlay, C. M. Gardiner, Canonical TGF-beta Signaling Pathway
828 Represses Human NK Cell Metabolism. *J Immunol* **200**, 3934-3941 (2018).
829 60. L. Das, A. D. Levine, TGF-beta inhibits IL-2 production and promotes cell cycle arrest in
830 TCR-activated effector/memory T cells in the presence of sustained TCR signal
831 transduction. *J Immunol* **180**, 1490-1498 (2008).
832 61. W. Chen, TGF-beta Regulation of T Cells. *Annu Rev Immunol* **41**, 483-512 (2023).
833 62. T. Yamazaki, A. J. Gunderson, M. Gilchrist, M. Whiteford, M. X. Kiely, A. Hayman, D.
834 O'Brien, R. Ahmad, J. V. Manchio, N. Fox, K. McCarty, M. Phillips, E. Brosnan, G. Vaccaro,
835 R. Li, M. Simon, E. Bernstein, M. McCormick, L. Yamasaki, Y. Wu, A. Drokin, T. Carnahan,
836 Y. To, W. L. Redmond, B. Lee, J. Louie, E. Hansen, M. C. Solhjem, J. Cramer, W. J. Urba, M.
837 J. Gough, M. R. Crittenden, K. H. Young, Galunisertib plus neoadjuvant
838 chemoradiotherapy in patients with locally advanced rectal cancer: a single-arm, phase 2
839 trial. *Lancet Oncol* **23**, 1189-1200 (2022).
840 63. J. J. Harding, R. K. Do, A. Yaqubie, A. Cleverly, Y. Zhao, I. Gueorguieva, M. Lahn, K. A.
841 Benhadji, R. K. Kelley, G. K. Abou-Alfa, Phase 1b study of galunisertib and ramucirumab
842 in patients with advanced hepatocellular carcinoma. *Cancer Med* **10**, 3059-3067 (2021).
843 64. R. K. Kelley, E. Gane, E. Assenat, J. Siebler, P. R. Galle, P. Merle, I. O. Hourmand, A.
844 Cleverly, Y. Zhao, I. Gueorguieva, M. Lahn, S. Faivre, K. A. Benhadji, G. Giannelli, A Phase
845 2 Study of Galunisertib (TGF-beta1 Receptor Type I Inhibitor) and Sorafenib in Patients
846 With Advanced Hepatocellular Carcinoma. *Clin Transl Gastroenterol* **10**, e00056 (2019).
847 65. D. Melisi, R. Garcia-Carbonero, T. Macarulla, D. Pezet, G. Deplanque, M. Fuchs, J. Trojan,
848 H. Oettle, M. Kozloff, A. Cleverly, C. Smith, S. T. Estrem, I. Gueorguieva, M. M. F. Lahn, A.
849 Blunt, K. A. Benhadji, J. Tabernero, Galunisertib plus gemcitabine vs. gemcitabine for
850 first-line treatment of patients with unresectable pancreatic cancer. *Br J Cancer* **119**,
851 1208-1214 (2018).
852 66. P. J. Santangelo, C. Cicala, S. N. Byrareddy, K. T. Ortiz, D. Little, K. E. Lindsay, S. Gumber, J.
853 J. Hong, K. Jelicic, K. A. Rogers, C. Zurla, F. Villinger, A. A. Ansari, A. S. Fauci, J. Arthos,
854 Early treatment of SIV+ macaques with an alpha(4)beta(7) mAb alters virus distribution
855 and preserves CD4(+) T cells in later stages of infection. *Mucosal Immunol* **11**, 932-946
856 (2018).
857 67. E. J. Fray, F. Wu, F. R. Simonetti, C. Zitzmann, N. Sambaturu, C. Molina-Paris, A. M.
858 Bender, P. T. Liu, J. D. Ventura, R. W. Wiseman, D. H. O'Connor, R. Geleziunas, T. Leitner,
859 R. M. Ribeiro, A. S. Perelson, D. H. Barouch, J. D. Siliciano, R. F. Siliciano, Antiretroviral
860 therapy reveals triphasic decay of intact SIV genomes and persistence of ancestral
861 variants. *Cell Host Microbe* **31**, 356-372 e355 (2023).
862 68. G. Escobar, D. Mangani, A. C. Anderson, T cell factor 1: A master regulator of the T cell
863 response in disease. *Sci Immunol* **5**, (2020).
864 69. R. L. Rutishauser, C. D. T. Deguit, J. Hiatt, F. Blaeschke, T. L. Roth, L. Wang, K. A. Raymond,
865 C. E. Starke, J. C. Mudd, W. Chen, C. Smullin, R. Matus-Nicodemos, R. Hoh, M. Krone, F.
866 M. Hecht, C. D. Pilcher, J. N. Martin, R. A. Koup, D. C. Douek, J. M. Brenchley, R. P. Sekaly,
867 S. K. Pillai, A. Marson, S. G. Deeks, J. M. McCune, P. W. Hunt, TCF-1 regulates HIV-specific
868 CD8+ T cell expansion capacity. *JCI Insight* **6**, (2021).

869 70. Y. S. Choi, J. A. Gullicksrud, S. Xing, Z. Zeng, Q. Shan, F. Li, P. E. Love, W. Peng, H. H. Xue, S.
870 Crotty, LEF-1 and TCF-1 orchestrate T(FH) differentiation by regulating differentiation
871 circuits upstream of the transcriptional repressor Bcl6. *Nat Immunol* **16**, 980-990 (2015).
872 71. S. G. Zheng, J. Wang, P. Wang, J. D. Gray, D. A. Horwitz, IL-2 is essential for TGF-beta to
873 convert naive CD4+CD25- cells to CD25+Foxp3+ regulatory T cells and for expansion of
874 these cells. *J Immunol* **178**, 2018-2027 (2007).
875 72. I. Frank, M. Cigoli, M. S. Arif, M. D. Fahlberg, S. Maldonado, G. Calenda, A. Pegu, E. S.
876 Yang, R. Rawi, G. Y. Chuang, H. Geng, C. Liu, T. Zhou, P. D. Kwong, J. Arthos, C. Cicala, B. F.
877 Grasperge, J. L. Blanchard, A. Gettie, C. M. Fennessey, B. F. Keele, M. Vaccari, T. J. Hope,
878 A. S. Fauci, J. R. Mascola, E. Martinelli, Blocking alpha4beta7 integrin delays viral
879 rebound in SHIVSF162P3-infected macaques treated with anti-HIV broadly neutralizing
880 antibodies. *Sci Transl Med* **13**, (2021).
881 73. M. Pertea, D. Kim, G. M. Pertea, J. T. Leek, S. L. Salzberg, Transcript-level expression
882 analysis of RNA-seq experiments with HISAT, StringTie and Ballgown. *Nat Protoc* **11**,
883 1650-1667 (2016).
884 74. M. I. Love, W. Huber, S. Anders, Moderated estimation of fold change and dispersion for
885 RNA-seq data with DESeq2. *Genome Biol* **15**, 550 (2014).
886

887

Acknowledgements

General: We acknowledge the helpful staff at the New Iberia Research Center as well as the help of Dr. Suchitra Swaminathan and the rest of the staff of the Flow Cytometry Core Facility at the Robert H. Lurie Comprehensive Cancer Center of Northwestern University in Chicago. Moreover, we thank the staff of the NUseq Core at Northwestern, and in particular Dr. Ching Man Wai and Matthew Schipma for the help with RNAseq data. Finally, we thank Dr. Lifson and the Leidos staff for viral load measurements as well as Dr. Laird at Accelevir for providing SIV-TILDA results in a timely manner. The content of this publication does not necessarily reflect the views or policies of the Department of Health and Human Services, nor does mention of trade names, commercial products, or organizations imply endorsement by the U.S. Government.

Funding: This project has been funded by National Institutes of Health grant R56AI157822 to Dr. Martinelli, the resource for NHP immune reagents to Dr. Villinger (R24 OD010947) for probe productions and in part with federal funds from the National Cancer Institute, National Institutes of Health, under Contract No. 75N91019D00024/HHSN261201500003I. The Lurie Cancer Center is supported in part by an NCI Cancer Center Support Grant #P30 CA060553.

Authors contributions: EM conceptualized the studies; JK performed and analyzed flow cytometry and immunePET/CT data; DB, MA, DF and SA collected and processed macaque samples; MRH generated vRNA/DNA and Elispot data; RC and MV analyzed Treg/Tfh; YT and TJH contributed to immunePET/CT analysis; EG, YG and EM analyzed RNAseq data; CMF, BK and RLR analyzed barcode data; JA, CC, FV and EM interpreted the data and wrote the manuscript.

Competing interests: The authors declare no competing interests.

Data and material availability: All data needed to evaluate the conclusions in the paper are included in the manuscript and/or the supplemental material. Transcriptional profiling data (raw RNAseq data) will be uploaded to GEO.

Figure Legends

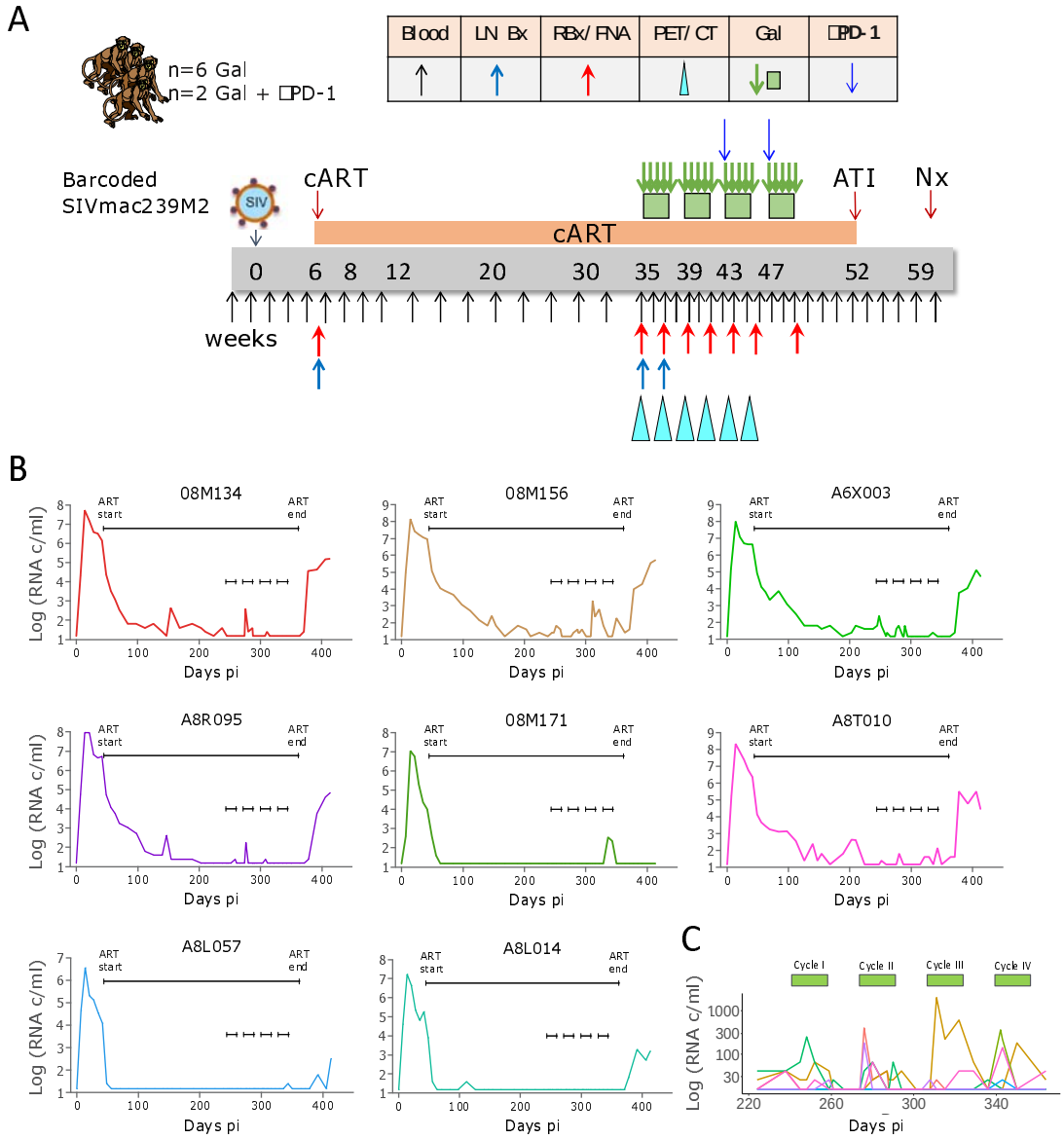

Figure 1. Four 2-weeks cycles with galunisertib lead to viral reactivation in blood. A) Schematic representation of the study and sampling schedule B) Plasma VL in blood for each macaque throughout the study. The longer black line indicates the period on ART, while the 4 small black lines indicate the start and end of each galunisertib cycle. C) Enlarged plasma VL for all macaques during galunisertib therapy. Green bars indicate galunisertib cycles.

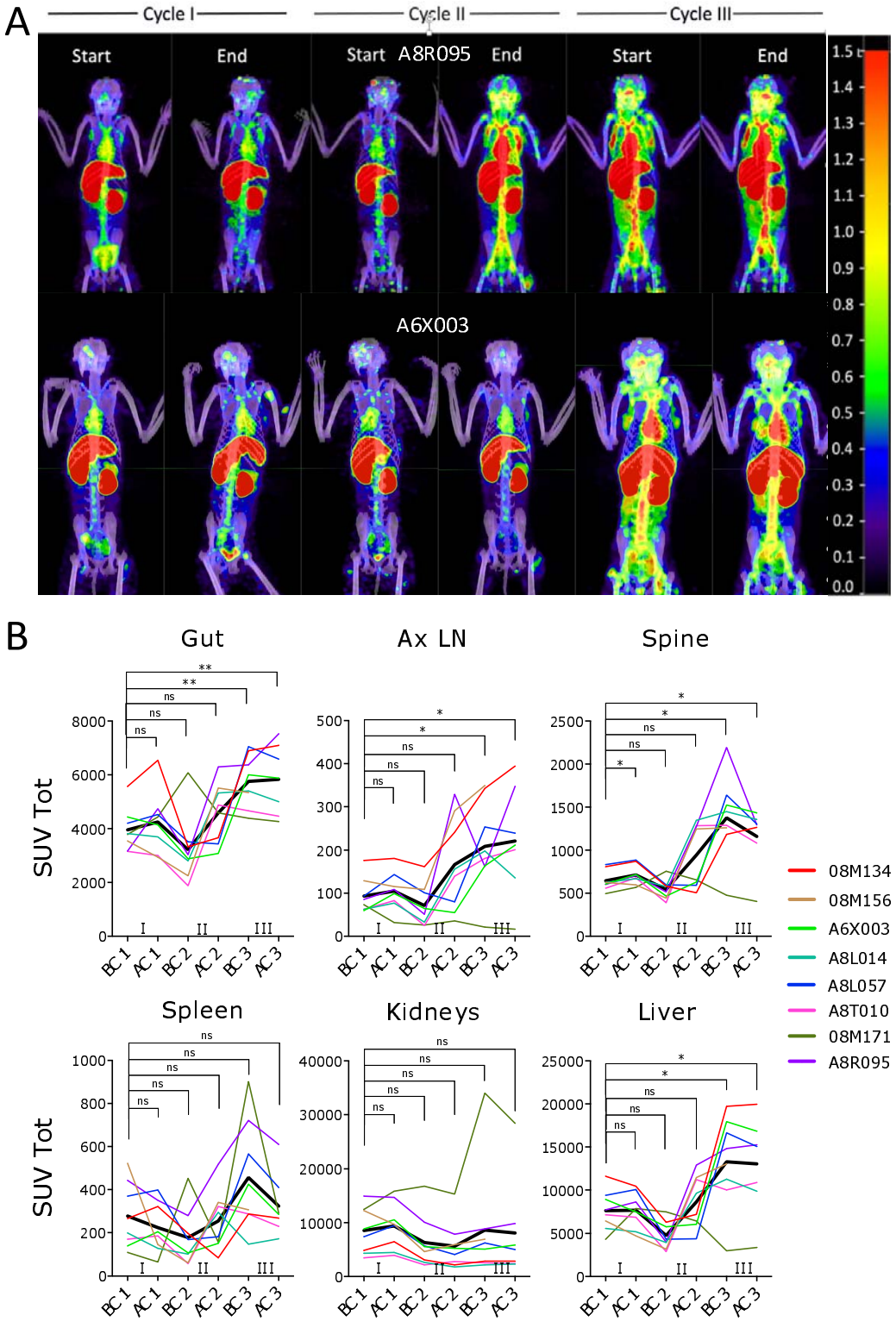

Figure 2. Galunisertib leads to viral reactivation in tissues. A) The ^{64}Cu-DOTA-Fab$_2$(7D3) probe was injected ~24hrs before PET/CT scan before and at the end of each of the first 3

galunisertib cycles. Representative images from the PET/CT scans are show for a macaque with a major increase at the end of cycle 2 and one showing increase at the beginning of cycle 3 B) Total SUV were calculated for each anatomical area and values analyzed with mixed-effect analysis. Thicker black line represents the mean. P–values were calculated for comparison of each time point with the before cycle 1 time point (BC1; AC1= after cycle 1, BC2= before cycle 2; AC2= after cycle 2; BC3= before cycle 3; AC3= after cycle 3; Holm-Sidak multiple comparison correction; *p≤0.05 **p≤0.01 ***p≤0.01)

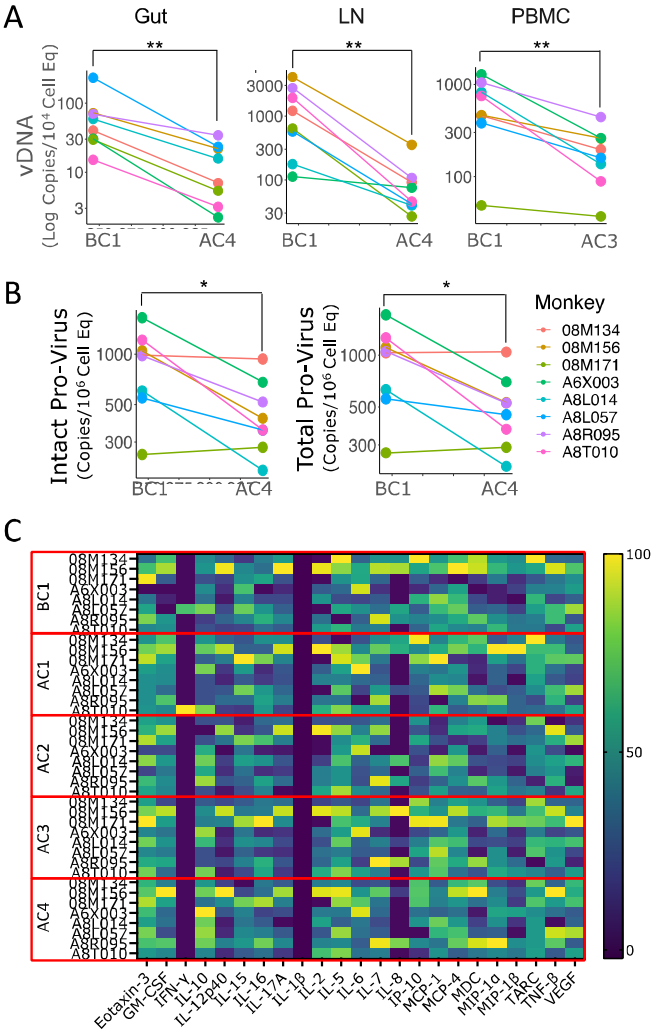

Figure 3. Galunisertib decreases viral reservoir in absence of systemic inflammation. A) Levels of cell-associated (CA)-vDNA per cell equivalent are shown for the time point before

cycle 1 (BC1) and at the end of cycle 3 (AC3) or 4 (AC4) for the respective tissues. B) IPDA data are shown for intact and total provirus for BC1 and AC4 in PBMC. pvalues are shown for Wilcoxon matched pair signed-rank non-parametric test (*p≤0.05 **p≤0.01 ***p≤0.01) C) Heat map of cytokine concentration in plasma at the indicated time point are shown after Log transformation and normalization. Statistical analysis was run on each factor separately and together (no significant differences after multiple comparison adjustment).

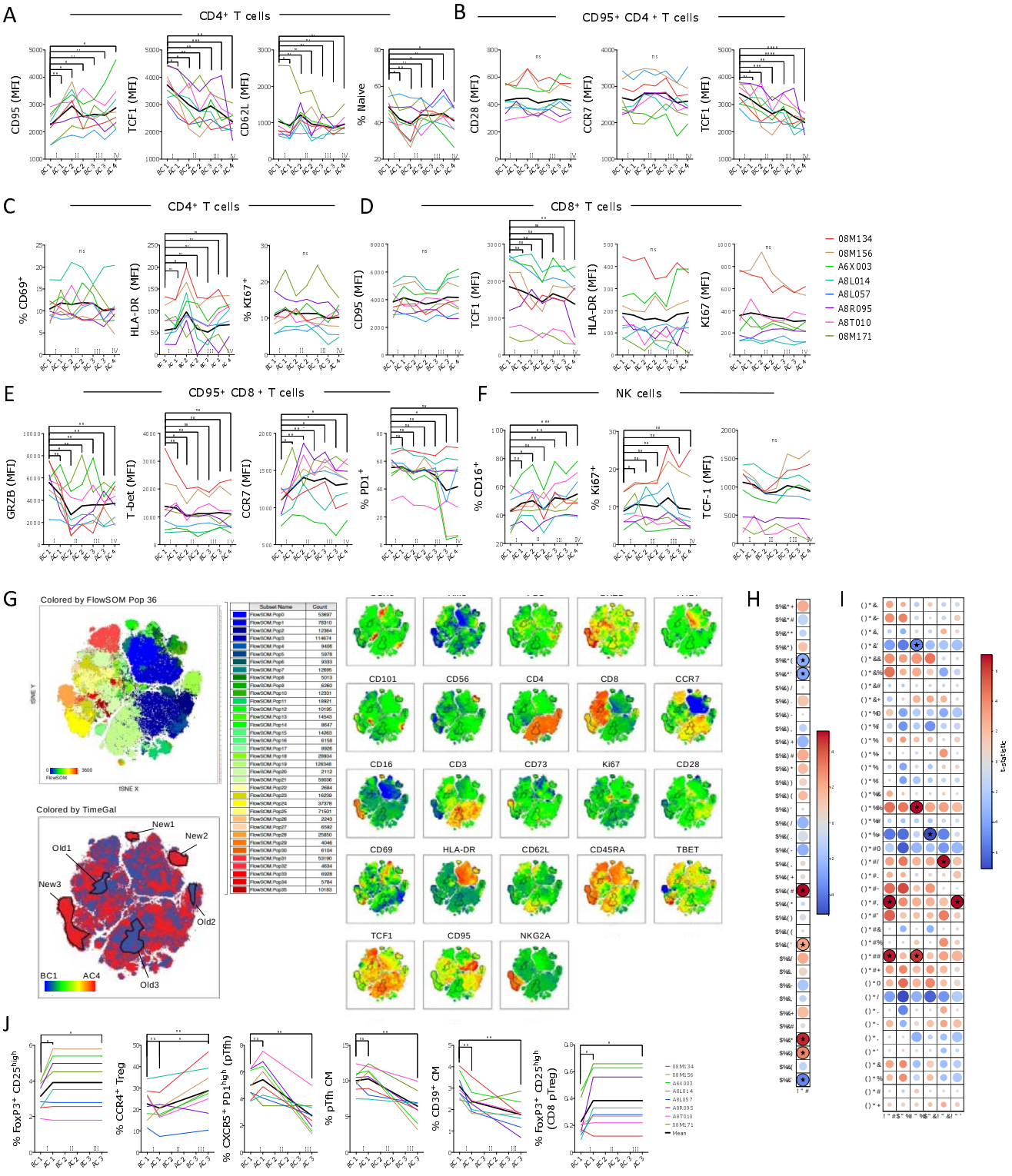
A
CD4+ T cells
CD95 (MFI)
TCF1 (MFI)
CD62L (MFI)
% Naive
B
CD95+ CD4 + T cells
CD28 (MFI)
CCR7 (MFI)
TCF1 (MFI)
C
CD4+ T cells
% CD69+
HLA-DR (MFI)
% Ki67+
D
CD8+ T cells
CD95 (MFI)
TCF1 (MFI)
HLA-DR (MFI)
Ki67 (MFI)
08M134
08M156
A6X003
A8L014
A8L057
A8R095
A8T010
08M171
E
CD95+ CD8 + T cells
GRZB (MFI)
T-bet (MFI)
CCR7 (MFI)
% PD1+
F
NK cells
% CD16+
% Ki67+
TCF-1 (MFI)
G
Colored by FlowSOM Pop 36
tSNE Y
tSNE X
FlowSOM
Colored by TimeGal
New1
New2
Old1
New3
Old2
Old3
BC1
AC4
CD101
CD56
CD4
CD8
CCR7
CD16
CD3
CD73
Ki67
CD28
CD69
HLA-DR
CD62L
CD45RA
TBET
TCF1
CD95
NKG2A
H
I
t-statistic
J
% FoxP3+ CD25high
% CCR4+ Treg
% CXCR5+ PD1high (pTfh)
% pTfh CM
% CD39+ CM
% FoxP3+ CD25high (CD8 pTreg)
08M134
08M156
A6X003
A8L014
A8L057
A8R095
A8T010
08M171
Mean

938

Figure 4. Galunisertib leads toward effector in T and NK cells, increasing Treg and decreasing Tfh frequencies. A-F) Geometric mean fluorescent intensities (MFI) of each marker and frequency of indicated subset within live, singlets $CD3^+$ $CD4^+$ T cells (A and C) or $CD3^+$ $CD4^+$ $CD95^+$ T cells (B) or $CD8^+$ or $CD8^+$ $CD95^+$ T cells or NK cells ($NKG2A^+$ $CD8^+$ $CD3^-$ cells) are shown. Thick black line represents the mean. Changes from baseline (beginning of cycle 1, BC1) are shown for graphs with at least 1 significant difference (Repeated measures ANOVA with Holm-Sidak correction; *p≤0.05 **p≤0.01 ***p≤0.01). G) tSNE of lymphocyte, live, singlets events after normalization for BC1 and AC4 (all 8 macaques) with FlowSOM 36 clusters overlaid on tSNE (top left) or heatmap of each markers MFI (right) or heatmap of time point (blue is BC1 and red is AC4; bottom left) is shown. 6 populations were manually gated on red or blue areas (red, New1-3 and blue Old1-3). H) Bubble chart displaying changes from BC1 in AC4. Color is proportional to the effect size and size to p-value (Wilcoxon sum rank non-parameter test). I) Bubble chart displaying changes from BC1 in all time point (ANOVA repeated measures with Holm-Sidak correction; *p≤0.05 **p≤0.01 ***p≤0.01). J) Frequency of indicated subset within live, singlets $CD3^+$ $CD4^+$ T or $CD3^+$ $CD4^+$ $CD95^+$ $CD28^+$ T cells (CM=central memory) or within $CD3^+$ $CD8^+$ T cells. Changes from baseline (BC1) are shown (ANOVA repeated measures with Holm-Sidak correction for multiple comparisons; *p≤0.05 **p≤0.01 ***p≤0.01).

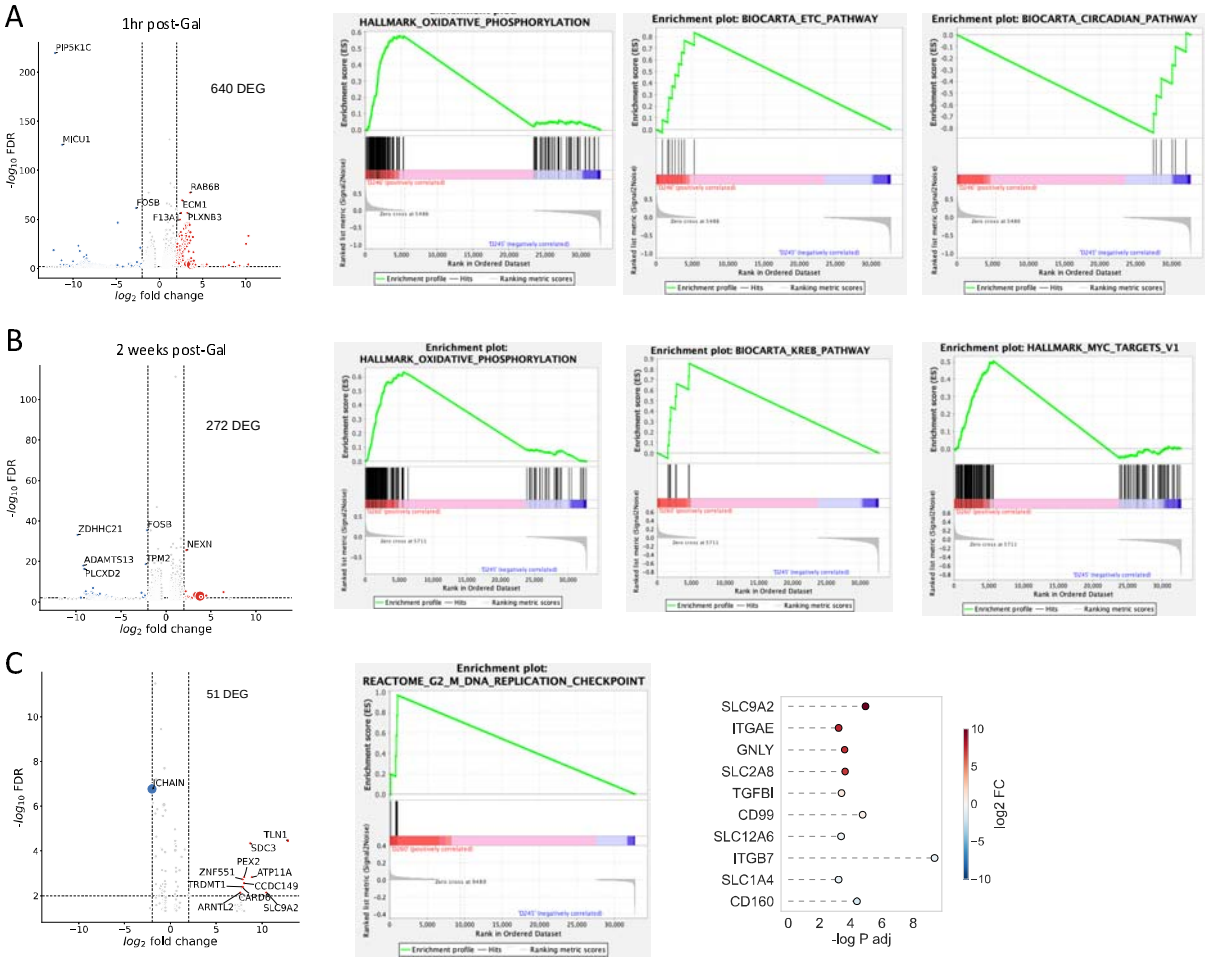

Figure 5. OXPHOS and other metabolic pathways increase rapidly with TGF-β blockade. A-C) Bulk RNAseq was performed with PBMC from before cycle 1 (24hrs) and 1hrs after the first dose of galunisertib (A) or after the last dose of cycle 1 (B) and with rectal biopsies collected before cycle 1 (24hrs) and after the last dose of cycle 1 (C). The number of differentially expressed genes (DEG) with an Adjpvalue <0.05 and $\log_2$FC>2and<-2 are shown in each respective volcano plot. Enrichment plots are shown after GSEA (with all adjp<0.05 DEGs) for significantly enriched pathways (top 1 or 2 pathway by ES). C) Lollipop graph of selected DEG of interest among significantly different genes (adjp<0.05).

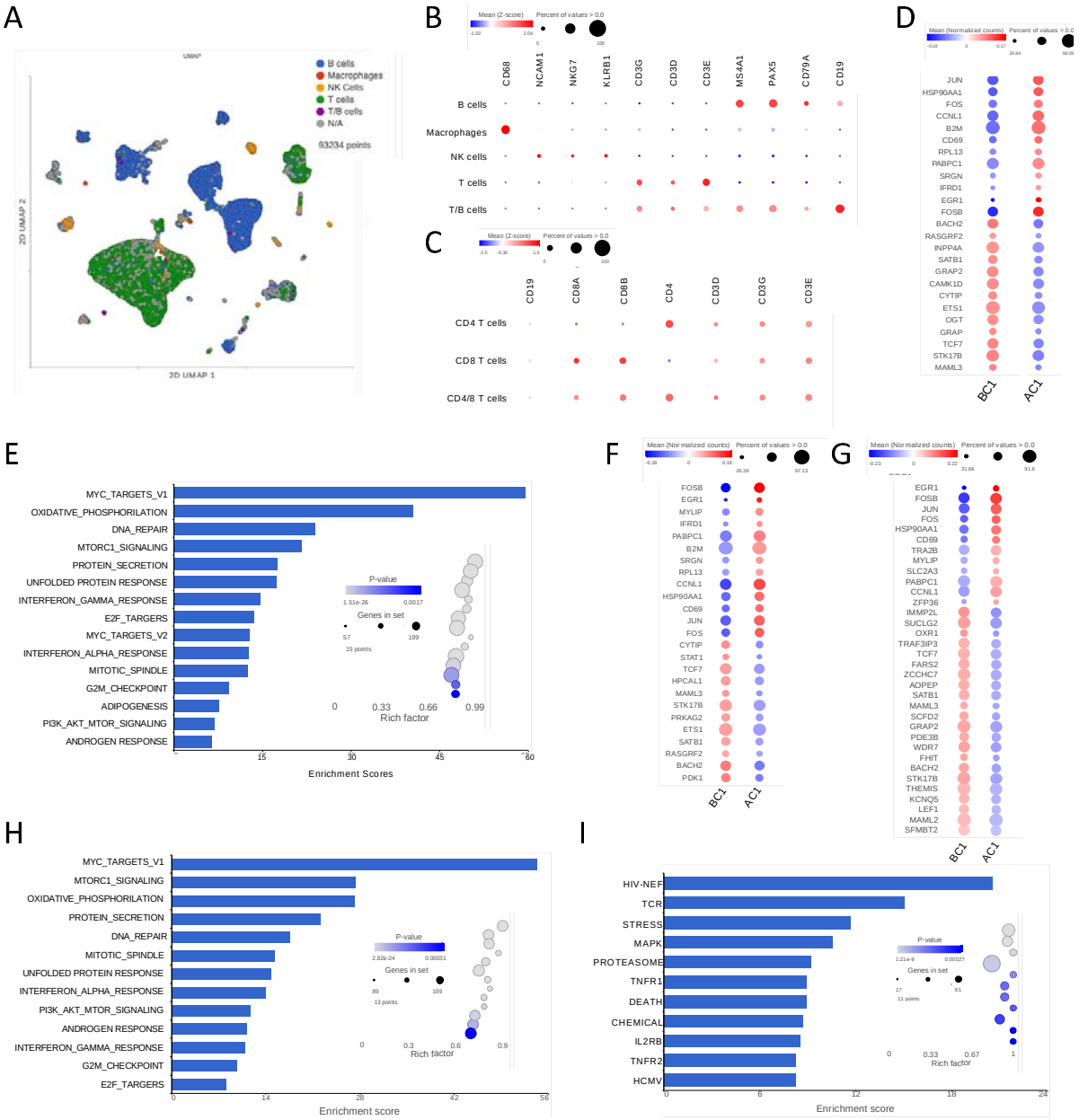

Figure 6. scRNAseq of lymph node before and after cycle 1 confirms a switch toward effector and increased metabolism in all immune subsets with galunisertib. A) UMAP projection of 93234 cells from lymph nodes collected right before and at the end of cycle 1 from all 8 macaques (16 samples). Gene-based classification of major immune subset is overlaid on UMAP. In gray are unclassified cells. B-C) Bubble plots showing expression (mean normalized counts proportional to the color; size proportional to the percentage of cells) of each marker

listed in each cell subset. Marker listed are those used for classification of major immune subsets (B) or CD4$^+$ and CD8$^+$ T cells (C). D) Significantly different genes (Adjp<0.05; log2FC=0.15) in the T cell subset are shown with color proportional to normalized counts. E) Significantly enriched pathways (adjp<0.01) in T cells DEGs within the hallmark collection. F-G) Significantly different genes (Adjp<0.05; log2FC=0.15) in the CD4$^+$ (F) and CD8$^+$ (G) T cell subset. H-I) Significantly enriched pathways (adjp<0.01) in CD4$^+$ T cells DEGs within the hallmark (H) and biocarta (I) collections.

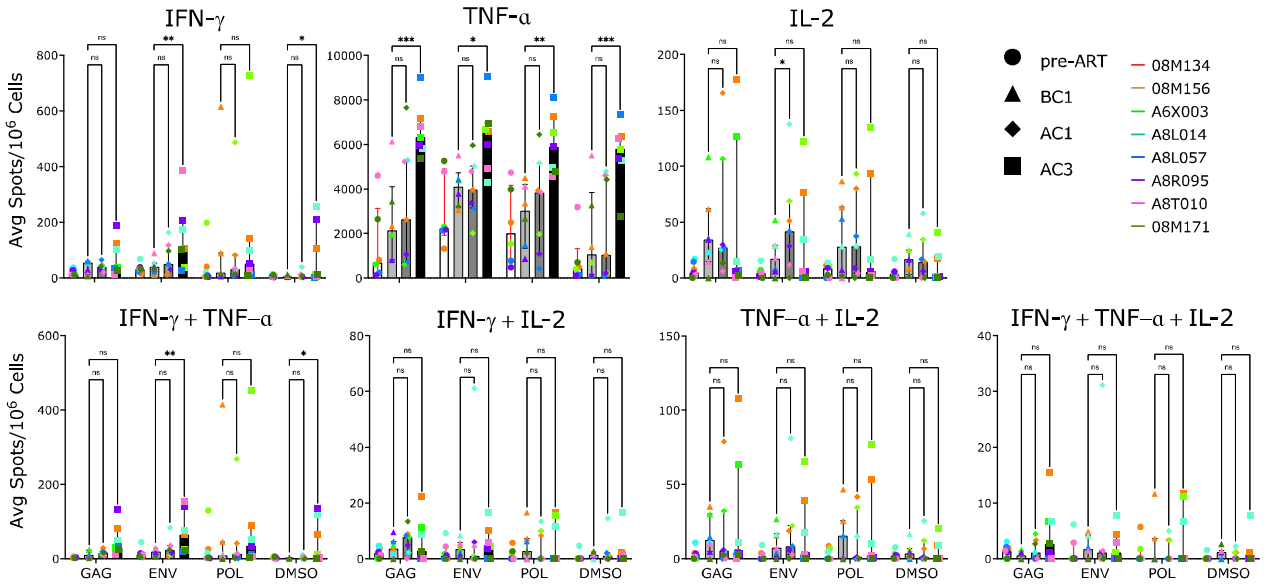

Figure 7. Galunisertib increases SIV-specific responses. Average spots (from triplicates) per 10^6 PBMC at the time of ART initiation (pre-ART), before cycle 1 (BC1), after cycle 1 (AC1) and at the end of cycle 3 (AC3) with galunisertib after 24hrs ex vivo stimulation with 15-mer peptides (gag, env, pol) or mock (DMSO). Each post-galunisertib time point was compared to BC1 (Mixed effect analysis with Dunnet post-hoc p-values are shown; *p≤0.05 **p≤0.01 ***p≤0.001)

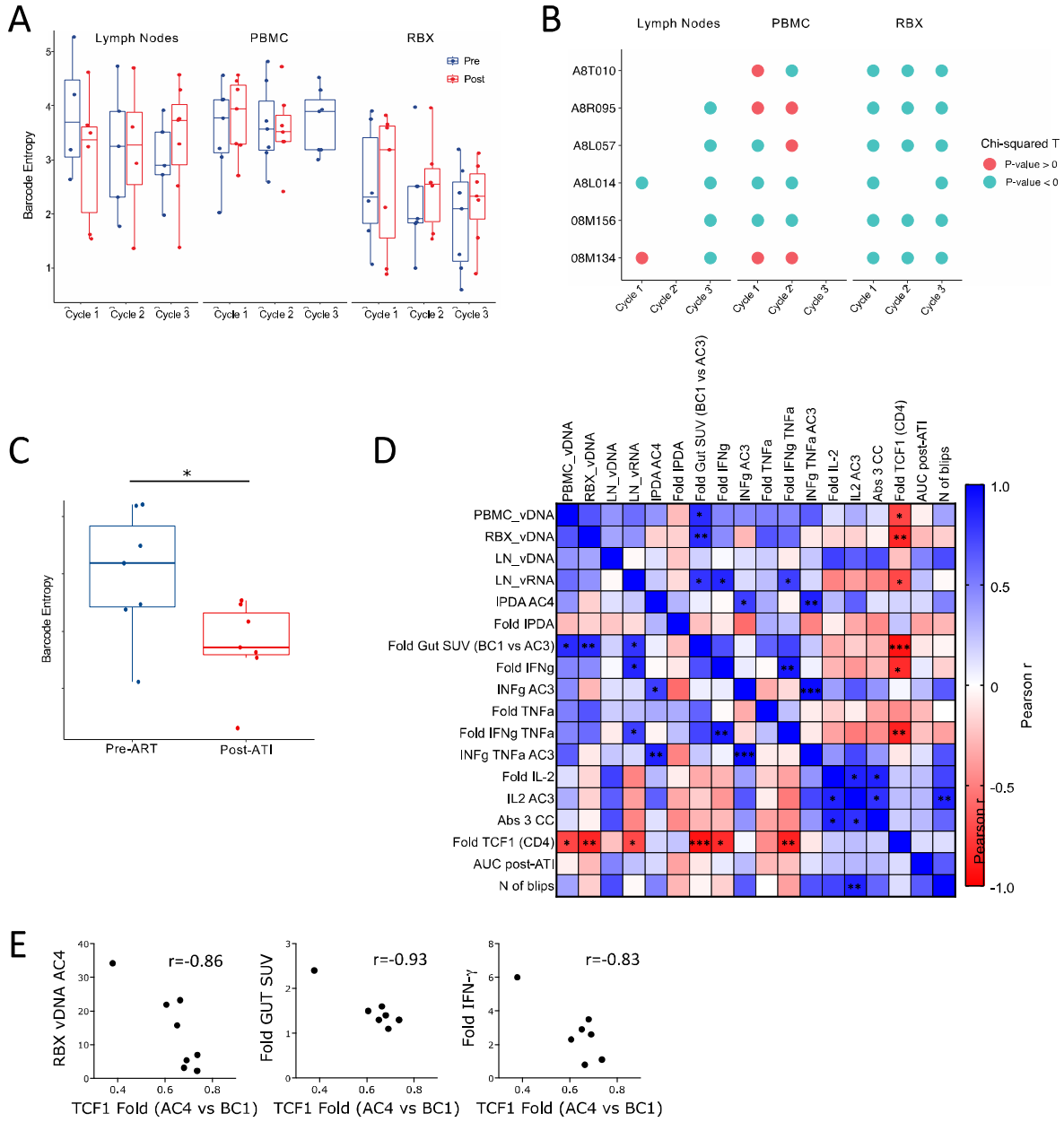

Figure 8. TCF1 decrease associates with virological and immunological endpoints. A) Barcode diversity measure as Shannon Entropy is shown before and after each of the first 3 galunisertib cycles for LN, PBMC and colorectal biopsies. Box-and-whisker plot represents the median +/− the interquartile range (no significant differences using linear mixed effects models). Blue= before; Red= end of each cycle. B) Bubble plot shows the results of statistical testing (Chi-squared) for differences in frequency distribution of barcodes before compared to after, for

each of the first 3 cycles of galunisertib for each macaque in the indicated tissues. Blue indicates significant differences $p \leq 0.05$. C) Barcode entropy of virus isolated at the time of ART initiation compared to week 6 post-ATI in plasma (Wilcoxon matched pairs test; $*p \leq 0.05$). D) Correlation matrix of several key variables of virological or immunological effect of galunisertib. Color is proportional to Pearson r coefficient. $*p \leq 0.05$ $**p \leq 0.01$ $***p \leq 0.001$ indicate significant correlations. F) Association between fold increase in TCF1 (MFI) from BC1 to AC4 with CA-vDNA levels at AC4, change in gut SUV at AC3 compared to BC1 and fold increase in IFN-γ (AC3 vs BC1). Person r is shown. All correlations have $*p \leq 0.05$.